NASA Contractor Report 187165
AIAA-91-2339

A Preliminary Characterization of Applied-Field MPD Thruster Plumes

Roger M. Myers
Sverdrup Technology, Inc.
Lewis Research Center Group
Brook Park, Ohio

David Wehrle
Cleveland State University
Cleveland, Ohio

Mark Vernyi
University of Akron
Akron, Ohio

James Biaglow
University of Cincinnati
Cincinnati, Ohio

Shawn Reese
Ohio University
Athens, Ohio

August 1991

Prepared for
Lewis Research Center
Under Contract NAS3-25266

National Aeronautics and
Space Administration

A Preliminary Characterization of Applied-Field MPD Thruster Plumes

Roger M. Myers[1]
Sverdrup Technology, Inc.
Lewis Research Center Group
Brook Park, Ohio 44142

David Wehrle[2]
Cleveland State University
Cleveland, Ohio 44115

Mark Vernyi[3]
University of Akron
Akron, Ohio 44325

James Biaglow[4]
University of Cincinnati
Cincinnati, Ohio 45221

Shawn Reese[5]
Ohio University
Athens, Ohio 45701

Abstract

Electric probes, quantitative imaging, and emission spectroscopy were used to study the plume characteristics of applied-field MPD thrusters. The measurements showed that the applied magnetic field plays the dominant role in establishing the plume structure, followed in importance by the cathode geometry and propellant. The anode radius had no measureable impact on the plume characteristics. For all cases studied the plume was highly ionized, though spectral lines of neutral species were always present. Centerline electron densities and temperatures ranged from 2×10^{18} to 8×10^{18} m^{-3} and from 7500 to 20,000 K, respectively. The plume was strongly confined by the magnetic field, with radial density gradients increasing monotonically with applied field strength. Plasma potential measurements show a strong effect of the magnetic field on the electrical conductivity and indicate the presence of radial current conduction in the plume.

---

[1]Propulsion engineer, member AIAA

[2]undergraduate student

[3]undergraduate student, member AIAA

[4]undergraduate student

[5]undergraduate student

Nomenclature

A_{ik}	transition probability, sec^{-1}
A_p	probe surface area, m^2
B_z	applied field strength at magnet exit plane, T
e	electron charge, C
E_u	energy of upper excited state, J
g_i	degeneracy of excited state
I_e	electron saturation current, A
I_p	probe current, A
I_{ik}	intensity, arbitrary units
J_d	discharge current, A
k	Boltzmann's constant, J/K
m_e	electron mass, kg
N	number density, m^{-3}
T	temperature, K
v	average particle speed, m/s
V_b	probe bias voltage, V
υ_{ik}	frequency of light from i - k transition, sec^{-1}

Introduction

Magnetoplasmadynamic (MPD) thrusters have demonstrated performance and power-handling capabilties which make them attractive for use as the primary propulsion system on orbit raising and planetary missions[1]. Thruster efficiencies over 40% and specific impulses over 5000 seconds have been demonstrated at power levels ranging from 30 kW to 5 MW, with the low-power thrusters operating in a steady-state mode and thrusters with powers over 500 kW operating in a pulsed, or quasi-steady mode, with test times of 1 - 2 milliseconds. While these performance levels might satisfy certain missions, there remain fundamental questions about the scaling of performance parameters with thruster power level, propellant, and the relationship between the quasi-steady thruster results and those obtained from steady-state thrusters. In addition, all of the high-performance data have been obtained from thrusters utilizing applied axial magnetic fields, and there is presently only a limited understanding of the physics of applied field thruster plasma acceleration.

A typical MPD thruster, shown in Fig. 1, consists of a central cathode with a coaxial, cylindrical anode. Propellant, injected through an insulating backplate, is heated, ionized, and accelerated via the interaction of the discharge current and the self-induced or applied magnetic field. This applied field is usually generated using solenoidal coils external to the anode.

While a substantial body of data exists concerning the plasma of self-field MPD

thrusters, little work has been done to characterize the impact of an externally applied field on the plasma properties. This is particularly important in light of recent results showing substantially improved performance with applied-field MPD thrusters[2-5]. Plasma property measurements can be used not only to study the scaling properties of the thrusters via the governing non-dimensional parameters, but they are also essential for verification of computer models. Quasi-steady testing permits insertion of diagnostic probes into the thrust chambers to make internal property measurements, but this is currently impossible with steady-state thrusters due to the extremely high heat fluxes experienced in the chamber. For this reason plasma property measurements in steady-state thrusters are usually confined to the plume region.

This paper presents the results of an effort to measure the global plasma characteristics in the plume of several applied-field MPD thrusters. Three diagnostics were used: emission spectroscopy, quantitative imaging, and electric probes. In Section II the experimental facility and thruster designs are briefly described, followed by a detailed discussion of the diagnostic techniques and their implementations. Results of the species identification, global ionic excited-state distribution, and electron temperature and density distribution measurements are presented in Section III. Finally, a brief discussion of the implications of the measurements for the dominant physics is given and the work summarized.

II. Experimental Apparatus and Procedures

Vacuum Facility and Power Supplies

The thruster test stand, shown in Fig. 2, was mounted in a 3 m diameter, 3 m long spool piece attached to a 7.6 m diameter, 21 m long vacuum chamber via a 3 m diameter gate valve. The facility was pumped by 19 oil diffusion pumps backed by three roots blowers and two mechanical pumps. The tank pressure was maintained below 0.07 Pa (5×10^{-4} Torr) indicated pressure during all tests. Details of the facility and performance diagnostics are given in Ref. 4-6.

The thrusters were powered using a set of six 66 kW Miller welding supplies connected in a series-parallel network providing up to 3000 amps at 130 volts. Typical thruster current and voltage ripples are shown in Fig. 3 for a thruster operating at approximately 15 kW. It is clear that the thruster discharge current and voltage had substantial ripple. The peak-to-peak amplitude for the case shown was 30%, though the ripple magnitude and frequency appeared to depend on both thruster geometry and operating conditions. The discharge currents and voltages reported in the following sections correspond to the mean values of these parameters. As discussed below this ripple had a large impact on the plume diagnostics.

Thruster and Applied Field Magnet Designs

A schematic of the MPD thrusters used in this study is shown in Fig. 1. The thrusters

consisted of water cooled, cylindrical copper anodes and coaxial, 2% thoriated tungsten cathodes. The chamber backplate material was boron nitride. Dimensions for the thrusters used in this study are given in Table 1. The letter designations correspond to those used in Ref. 4, where performance results for these tests are given. The cathodes for all geometries except G and I had hemispherical tips. The cathode for geometry G was conical. The hollow cathode used in geometry I has a flat tip. Propellant, either argon or an argon-hydrogen mixture, was injected through an annulus at the cathode base and through holes near the chamber midradius. These injector holes were spaced 15 degrees apart to ensure a relatively uniform azimuthal propellant distribution.

The applied magnetic fields were generated using a solenoid external to the anode. To accomodate the various thruster sizes and maximize the potential applied field strength with each thruster, two solenoids, 15.3 and 20.3 cm in bore diameter, were needed. These solenoids generated magnetic fields ranging from 0 to 0.2 Tesla at the centerline of the magnet exit plane. All geometries except C, E, and F were tested with the 15.3 cm I.D. magnet. Calculated magnetic field strengths are shown as a function of axial distance from the exit plane for the 15.3 cm I.D. magnet at a current of 1400 amps in Fig. 4. These calculations have been compared with detailed measurements made of the field strength and showed good agreement. The measurements showed that the fields scale linearly with magnet current, yielding field strengths at the center of the exit plane of 1.66×10^{-4} Tesla/amp and 8.48×10^{-5} Tesla/amp for the 15.3 and 20.3 cm diameter magnets, respectively. For this study the MPD thrusters were mounted with the anode exit plane flush with the end of the solenoid. All magnetic field strengths, B_z, reported below refer to its value at the centerline of the magnet exit plane.

Plume Diagnostics and Data Reduction

Emission spectroscopy, quantitative plume imaging, and electric probes were used to characterize the thruster plume. Results from each of these independent measurements were compared to evaluate the plume physics.

The emission spectroscopy measurements were made using a 1.25 m Czerny-Turner spectrometer. The spectrometer was equipped with a 2400 grooves/mm grating blazed at 500 nm and an intensified 1024 diode linear array detector. The optical arrangement, shown in Fig. 5, imaged the thruster plume onto the spectrometer entrance slit and provided the flexibility to make measurements at a variety of axial and radial locations. The spectral resolution was approximately 0.008 nm per pixel, depending slightly on the wavelength. The data reported here were taken 5 mm from the anode exit plane across the centerline of the thruster. Results were used to identify the plume species and obtain preliminary excitation temperatures using line-of-sight integrated line intensity ratios.

These single-point, line-of-sight integrated results were used to identify spectral regions of interest for plume imaging. Relative distributions of excited states were obtained using a CID camera with an image acquisition board and software. The control software automatically moved a stepper-motor driven filter wheel to preselected filters and acquired a

preset number of images with each filter. For this work two filters were used: one centered at 488.0 nm with a 1 nm bandpass, and a second centered at 514.7 nm with a 0.8 nm bandpass. Both filters pass only light from argon ion transitions. Each picture consisted of 493 columns and 461 rows of pixels with 8-bit intensity resolution. The line-of-sight intensity integrals recorded in these images were reduced to radial emission coefficient profiles using the Abel inversion technique developed by Sudharsanan[7]. No intensity calibration was performed on the optical system, so that only relative values were obtained.

The Abel-inversion software loaded an image, interactively found the thruster exit plane, automatically identified the plume region, and performed the inversion on the maximum number of columns possible within the constraints of the plotting software. The plume region was identified in order to maximize the spatial resolution within the luminous plume and prevent inversion of dark regions. The plotting package limited the number of columns to 54, which typically corresponded to a spatial resolution in the axial direction of 0.1cm. The Abel integral equation was solved for each column of intensity profiles by a multistep process. First, the discrete Fourier transform (DFT) of the intensity profile was computed using a fast-Fourier transform algorithm. No attempt was made to reduce signal noise. The axis of symmetry of the data was determined by minimizing the imaginary component of the DFT. This component was then set equal to zero to force symmetry for the inversion. The inverse Hankel transform was then applied to the shifted Fourier transformed input profile to yield the relative emission coefficient for the observed transition as a function of radius. Inversion of 54 columns required about 40 minutes on a 386-based personal computer. The inversion routine was verified with several known test functions[8]. However, all of these test functions had on-axis peaks, while much of the experimental data consisted of profiles with off-axis peaks. No test functions were found which could be used to verify the validity of the algorithm under those conditions.

Interpretation of the spectroscopic and plume-imaging results required quantitative distributions of electron density and temperature. These were obtained using electric probes. A fast-moving, probe-positioning system was mounted in front of the thrust stand as shown in Fig. 2. This probe positioning system, shown schematically in Fig. 6, had the capability of holding four probes and providing 91 cm of radial motion and 30 cm of axial motion with linear tables, both driven by computer-controlled stepper motors. The tables were covered with water cooled copper sheet to prevent them from over-heating during thruster operation. After moving to the preset axial postion, the probes were moved radially through the plume at a constant velocity of 30 cm/sec with acceleration and deceleration phases near the ends of the traverse.

A single 0.7 cm long, 0.013 cm diameter, electric probe was used for these measurements. The probe dimensions were selected to minimize end-effects, reduce peak saturation currents, and permit the use of thin-sheath theory for the data reduction[9,10]. The probe was mounted in a 0.1 cm diameter, 4 cm long, alumina tube which was glued into the end of an L-shaped, water-cooled, stainless-steel tube with ceramic adhesive. Triangular braces were attached to the vertical portion of the steel tube to minimize vibration while the probe was in

motion. Water cooling was required only along the vertical portion of the probe support to prevent melting of the wire insulation. Tungsten wire and ceramic insulation were used near the probe tip, rather than water cooling, in order to minimize the probe cross-section.

A test was performed to establish the impact of surface contaminants on the probe response. The probes were cleaned during the pump down of the 3 m diameter spool piece using an 800 V, 0.5 mA glow discharge between the probe tips and an electrode placed approximately 8 cm away from the tips. The area around the probes was flooded with argon in an effort to prevent residual air from damaging the surface. During testing with the cleaned probes no evidence of signal degradation was observed, indicating probe-surface contamination had little effect on the measurements. The probe-bias circuit, described below, was left on throughout all tests, so that some probe cleaning would take place between periods of data acquisition.

The probe was biased with respect to facility ground (the vacuum tank wall) using a bipolar amplifier driven by a function generator. The function generator provided a continuous triangular wave at 135 Hz, which the bipolar supply amplified to +/- 15 volts. The circuit is shown in Fig. 7. The triangle-wave frequency was chosen to minimize the time over which the probe had to sustain the electron saturation current and to provide one complete voltage - current characteristic for the probe every 1 mm of radial motion. Several tests were performed to verify the frequency response of the probe electronics, and no distortions were measurable below 500 Hz.

The software used to control probe motion permitted automatic scanning of the plume properties. The axial distances from the thruster at which radial profiles were to be taken were preselected and the entire data-acquisition sequence was performed automatically. Probe current and voltage data were collected continuously at either 76 or 150 kHz during the radial traverse and stored once the traverse was completed. Either 50,000 or 100,000 data sets were taken each traverse, corresponding to either 500 or 1000 full voltage - current characteristics for probe. The large number of points per ramp were required to properly curve fit the data during data reduction. The resulting large data sets required up to 3 minutes to store, and limited the number of radial distributions obtained at a given operating condition. In addition, the very high heat fluxes experienced by the probes precluded regular measurements closer than 15 cm from the thruster, though some passes were made as close as 6 cm.

The electric-probe data were automatically reduced using software which loaded in the continuous voltage and current signals, isolated the individual V_b - I_p characteristics, performed the required curve fits, and stored the results. The software permitted selection of the portion of the radial profile to be reduced and automatically plotted the raw data and the curve fits to the semi-log plots used to calculate the electron density, temperature, and the plasma potential. Simple electric-probe theory[9,10] was used to reduce the data, and no attempt was made to account for the effect of the applied magnetic field. Neglecting the effects of the applied magnetic field was justified by considering the ratio of the electron gyro radius to the probe radius[10]. For all data shown except that collected less than 10 cm from the thruster

exit plane this ratio was greater than five, values for which the magnetic field effects should be small. In this simple analysis, the electron temperatures and densities were obtained from

$$T_e = \frac{e}{k}\left(\frac{d\ln(I_p)}{dV_b}\right)^{-1}; \qquad N_e = \frac{I_e}{eA_p\sqrt{T_e/2\pi m_e}} \qquad (1)$$

The plasma potential was established by finding the intersection of the lines curve-fit to the electron-saturation and electron-repelling regions of the probe characteristic. The plots of the characteristics were needed to verify that appropriate ranges of the V_b - I_p characteristic were used for the curve fits. This was especially important because the criteria used to select these ranges had to be valid for regions in the plume with densities differing by almost two orders-of-magnitude.

III. Experimental Results

An MPD thruster test was initiated by setting the propellant flow rate, turning on the applied field, and using a set of countdown timers to turn on the main power supply, inject a burst of propellant into the chamber, and cycle the high voltage ignitor. The first 1 - 3 seconds of the test were characterized by particulate emission and substantial fluctuations in the plume. No attempt was made to characterize the start-up behavior as a function of the initial operating condition. Once the discharge had stabilized, data collection began. The thruster was allowed to remain at one operating condition, defined by the propellant flow rate, discharge current, and applied-field strength, for several minutes to insure stability. Operating points were always repeated at least twice over long intervals to ensure reproducibilty of the terminal characteristics and performance. The complexity and time required for the plume diagnostics precluded a highly systematic study of plume characteristics as functions of geometry, propellant, flow rate, discharge current, and applied-field strength. However, sufficient data were obtained to establish trends and begin to identify the plasma characteristics. These trends are discussed in the following sections. Note that only the hollow-cathode thruster, geometry I in Table 1, could be succesfully tested with no applied magnetic field. For all other geometries turning off the applied-field magnet resulted in very unstable operation with severe particulate ejection.

Plume Species

Plume species were identified by comparing measured spectra with tabulations in Ref. 11. Spectra were collected at 333.6, 356.0, 362.6, 407.2, 420.0, 433.3, and 488.8 nm with a band width of 8.19 nm. Figure 8 shows a typical spectrum collected at 356 nm where several singly-ionized argon lines are identified. Listed in Table 2 are the plasma species and dominant spectral lines identified from these spectra. The argon and hydrogen lines were only observed when those species were used as a propellant. The copper and tungsten lines were most evident at either high discharge current or high magnetic-field strength. While considerable effort was made to find doubly-ionized argon lines, none were found. Neutral argon lines, though weak, were evident for all operating conditions. As shown in Fig. 9, for a

test with hydrogen propellant on geometry A, the peak H_β line intensity increased linearly with applied-field strength. It was not possible to obtain more detailed correlations of line intensities with thruster operating conditions due to the limited number of data sets.

Density and Temperature Distributions

Preliminary estimates of the electron temperature near the thruster exit plane were obtained assuming that the excited-state populations followed a Boltzmann distribution. Using this assumption, the temperature was obtained from

$$T_e = \frac{1}{k(E_i - E_j)} \ln\left(\frac{I_{ik} g_j A_{j1} \nu_{j1}}{I_{j1} g_i A_{ik} \nu_{ik}}\right) \qquad (2)$$

Improved estimates of the temperature were obtained by plotting the logarithmic term in Eqn. 2 vs. the difference in upper excited state energies, where the temperature is proportional to the slope of the linear least-squares fit to the data. A typical example of this process is shown in Fig. 10. The data used in this analysis were the line-of-sight integrated line intensities for the spectral lines listed in Table 3. The data shown were obtained 0.5 cm from the exit plane of thruster geometry C using 0.1 g/s argon propellant at a discharge current of 1000 A, and with an applied field strength of 0.051 T. Values for transition probabilities, energy levels and degeneracies were obtained from Ref. 11. The adequacy of the linear curve fit justified use of the Boltzmann distribution. The electron temperature for the case shown, obtained from the inverse of the slope, was 12,200 K. Results obtained at applied-field strengths of 0.051, 0.038, and 0.034 T showed no dependence of the electron temperature on applied-field strength.

Photographic studies of the plume showed that a very pronounced structure existed with the applied field. Shown in Fig. 11 are raw intensity profiles of the 488 nm argon ion transition at three axial distances from thruster geometry E with a discharge current of 1250 A, an applied field of 0.042 T, and an argon flow rate of 0.1 g/s. It is apparent that a cone of high luminosity propagates from just outside the cathode diameter with a minimum along the centerline. Outside the cone there is a plateau of constant luminosity followed by a rapid decrease in intensity to the background level. The intensity of the plume decreased in the axial direction and the cone radius increased slightly. A similar structure was observed with both the 514.7 nm filter and unfiltered images, and the structure disappeared when the applied-magnetic field was turned off. A series of similar images were Abel inverted to extract the actual radial dependence of the emission coefficient and correlate this with thruster geometry and operating conditions.

The effect of the applied-field stength on the plume structure for geometry C is shown in Fig. 12a and b. These are contour plots of the relative-emission coefficient in the plume for the 514.7 nm argon ion line. The emission coefficient is directly proportional to the number density of the upper excited state of the transition, and is dependent on both the ground state density of argon ions and the excitation/de-excitation rates in the plume. The thruster would be to the left of the plots, with the exit plane at an axial position of zero, and

the cathode tip at the (0,0) location. The lines of constant emission coefficient do not intersect the thruster exit plane (the y - axis) due to the limitations of the plotting package. The presence of the high-luminosity cone is obvious, and it appears that the plasma near the cathode tip does not contribute significantly to the plume luminosity. From the two figures it is clear that increasing the applied-field strength from .025 to 0.064 Tesla approximately doubled both the peak emission coefficient and the axial extent of a given emission coefficient. Note that the inner radius of the cone, ~ 0.7 cm, corresponds closely with the cathode radius of 0.64 cm, and that the the inner surface of the cone appears to slowly diverge in the downstream direction. The influence of the discharge current on the 514.7 nm emission coefficient is shown in Fig. 13a and b for currents of 750 and 1500 amps. For both cases there were significant off-axis peaks in the emission coefficient, but at the higher currents the plasma in front of the cathode contributed significantly to the luminosity, whereas it did not at the low currents.

To check whether the correlation of the plume-luminosity distribution with the cathode radius was spurious, a test was performed with a 1.27 cm radius cathode with the same anode dimensions (geometry E). Shown in Fig. 14 is a contour plot of 487.9 nm emission coefficient for this thruster with an applied magnetic field of 0.030 Tesla. It is clear that for this geometry the luminous cone had an inner radius of ~ 1.5 cm, showing that the cone did arise from the cathode surface. A final check on the influence of cathode geometry on the excited state distribution in the plume was performed by shortening the cathode. The thrusters, geometries B and G in Table 1, had anode and cathode radii of 3.81 and 0.64 cm, respectively, and cathode lengths of 7.6 and 2.5 cm. The cathode used in geometry G had a conical, non-hemispherical, tip. As can be seen from Fig. 15a the plume for the long cathode test (geometry B) had a similar structure as that for thruster with the large anode radius (geometry C) shown in Fig. 12, indicating that anode radius did not have a fundamental effect on the plume characteristics. However, a dramatic difference is seen in Fig. 15b with the short, conical-cathode thruster. For the short cathode, the plume intensity peaked along the centerline and decreased mononotically for increasing radius, no longer showing the high-luminosity cone.

The influence of propellant on the plume-species distribution was studied by adding small quantities of hydrogen (1 to 10%) to the argon. This increased the terminal voltage and subtantially changed the plume characteristics. As shown in Figures 16a and b, adding hydrogen not only increased the intensity of the 488 nm emission but also changed its distribution, with the luminosity now substantially more concentrated near the center. To eliminate the possibility of the 486.1 nm H_β line contributing to the intensity measured with a 488 nm filter, several checks with pure hydrogen were performed. In none of these experiments was H_β emission detected through the 488 nm filter.

Electron-density and temperature measurements were made using single electric probes swept through the plume to identify the causes for the observed plume structure and its dependence on the thruster geometry and operating conditions. These measurements were complicated by the large ripple in the thruster current and voltage shown in Fig. 3, which

induced corresponding fluctuations in the electron density and temperature. Raw probe current and voltage signals taken at a reduced probe-bias power supply frequency of 13.5 Hz (27 V-I characteristics/second) are shown in Fig. 17. These data were taken with the hollow-cathode thruster (geometry I) outside the main plume to reduce power to the probes resulting from maintaining the electron-saturation currents for these extended periods (see discussion in Section II). The probe was biased between +/- 17 volts. The probe current was near zero in the ion-saturation region and reached a peak of - 0.013 amps in the electron-saturation region. As the probe current increased, the large thruster current and voltage ripples began to impact the signal. The effect peaked at ~ 30% ripple of the mean electron-saturation current. The magnitude of the probe-current ripple was comparable to the 30% discharge current ripple observed during the test (Fig. 3). The frequencies were different, however, with the power supply oscillating at ~ 450 Hz and the electron saturation current at ~ 360 Hz.

During data acquisition the ramp frequency of the bias voltage was 135 Hz, or an order-of-magnitude higher than that used in the above described test. While this prevented large fluctuations from appearing in the electron saturation current of a given V - I characteristic, over a series of ramps the values did fluctuate by the same 30% previously measured. Shown in Fig. 18 are raw, probe-voltage and current signals taken at one location over 0.03 seconds. It is evident that the electron-saturation current fluctuated significantly over the course of the measurements. These fluctuations were the principal source of scatter in the electron density and temperature measurements presented next.

Shown in Fig. 19a and b are radial electron density profiles taken 15 and 35 cm away from the hollow-cathode thruster, geometry I, both with and without an applied-magnetic field. For both cases the propellant flow rate was 0.15 g/s argon and the discharge current was 1000 A. The confining effect of the applied field is evident. The centerline densities with B_z = 0.1 T were significantly higher than those for B_z = 0, and the radial density profile with the applied field had a flat-topped central region followed by a very rapid decrease in density. Specifically, 15 cm from the thruster, the density for the case without an applied field drops from a peak of ~ 2 x 10^{18} m^{-3} on center to 4 x 10^{17} m^{-3} at a radius of 30 cm, while with the applied field, the density was approximately constant at 4 x 10^{18} m^{-3} for the inner 7 cm, but decreased to 1 x 10^{17} m^{-3} by a radius of 12 cm. Comparing the two cases in terms of the observed radial number density gradients, it appears that the applied field maintained a gradient of ~ 9 x 10^{19} m^{-4}, while without the applied field this dropped by an order-of-magnitude to 6.6 x 10^{18} m^{-4}. In addition, the rate at which the density decreased with increasing axial distance was much lower with the applied field than without it. At 15 cm from the thrusters the centerline densities were comparable both with and without the field, but 35 cm away the density with the field was six times greater than for the case with no applied field. These trends continued when the applied field strength was increased, but the changes were less dramatic. Shown in Fig. 20 are electron density profiles obtained 35 cm from thruster geometry F with a discharge current of 1000 A, an argon flow rate of 0.1 g/s, and with applied fields of 0.030 and 0.12 Tesla. The centerline electron density did not change significantly for the two field strengths, though the radial profile was much sharper with the higher applied field. The electron densities differed by almost an order of magnitude at a

radius of 20 cm, showing that the higher field sustained much steeper radial density gradients.

The effect of the discharge current on the electron density profiles for zero applied magnetic field is shown in Fig. 21. These data were taken 25 cm from the hollow-cathode thruster, geometry I, at an argon mass flow rate of 0.15 g/s. The centerline density increased from ~ 1 x 10^{18} m^{-3} at a current of 1000 A to ~ 4 x 10^{18} m^{-3} at a current of 1500 A. However, increasing the discharge current did not dramatically change the the radial density profile, but rather increased the density across the entire profile.

The high luminosity cone observed using the imaging was not reflected in the electron density profiles shown above, though the profiles for cases with an applied magnetic field did have relatively broad, flat-topped peaks. While off-axis peaks corresponding to the luminosity cone did appear in the radial profiles of the electron saturation currents, they appear to reflect changes in the electron temperature rather than the density. Shown in Fig. 22 is the radial temperature profile for geometry B taken 25 cm from the thruster with a discharge current of 1000 A, an applied field of 0.1 T, and an argon flow rate of 0.1 g/s. The relatively flat-topped density profiles are in sharp contrast to the off-axis peaks seen in the temperature results. The temperature reached a minimum of ~10,000 K on centerline, increased to a peak of ~ 17,000 K at a radius of 5 cm, decreased to ~ 12,000 K and then rose monotonically at higher radii. Note that these magnitudes are consistent with the 12,200 K obtained spectroscopically. The increase in scatter at the larger radii was due to a decrease in signal-to-noise ratio as the electron density decreased. The cause for the increase in temperature at higher radii is not known, though it may have been due to the higher radial diffusion rates of the higher energy electrons. It is unlikely that the temperature increase was a result of an increase in probe angle with respect to the flow, as this parameter has been shown not to affect single probe temperature measurements. While it may have been an error due to the presence of the B_r and B_z components of applied-magnetic field intersecting the probe tip, no mechanism has been found which would explain the result. The same increase in temperature was observed at the lowest applied field strengths at the farthest axial distances from the thruster, cases for which the electron gyro radius was more than 50 times the probe radius. In addition, experiments performed using a triple electric-probe technique[12] showed the similar radial electron temperature profiles, indicating that the result was not due to the data reduction technique.

The effect of the applied field on the electron temperature for the hollow cathode thruster is illustrated in Fig. 23, which compares the results for B_z = 0 and B_z = 0.1 T at an axial position 15 cm away from the thruster. It is clear that the centerline temperatures of about 7500 K are unaffected by the applied field while the temperature at increasing radii rises rapidly for the high applied field and is flat for the case of zero applied-field. The axial temperature distribution for the case with the applied field is shown in Fig. 24. Much as was found with the electron density, the centerline temperature did not change significantly from 15 to 35 cm away from the thruster, though the radial distributions showed a substantial drop in temperature at higher radii. The axial temperature distribution for thruster geometry I with no applied-field showed no significant changes, and increasing the discharge current from

1000 to 2000 A without an applied field had no measurable effect on the electron temperature.

It was shown earlier using the images (Figures 12 - 16) that the cathode length had a dramatic effect on the plume luminosity distribution (density distribution of upper excited states). The corresponding comparisons of electron density and temperature measurements are shown in Figures 25a and b. The cathode length had little effect on the electron density distribution at 25 cm, but the temperature distribution with the short cathode is peaked on the centerline without the off-axis peaks exhibited by the long cathode.

The influence of thruster geometry and operating conditions on the plume is also evident in the behavior of the plasma potential. As discussed above, the electric probe was biased relative to the vacuum facility wall, so that all reported potentials are with respect to facility ground, not the thruster electrodes. However, for all operating conditions for thrusters with long cathodes (geometries A, B, C, D, E, F, and I), the cathode was between 0 and -1 V from facility ground. Only with the short-cathode thruster (geometry G) was the cathode not close to ground potential, reaching a value of -15.5 V with respect to ground.

Figure 26 shows the influence of the applied magnetic field on the plasma potential distribution. For the zero-field case studied with the hollow-cathode thruster shown in Fig. 26a, the plasma potential was flat and near zero throughout the plume, whereas when a magnetic field of 0.041 T was applied, the potential increased by 3 to 5 volts and showed a slight minima near the centerline. This trend continued with higher magnetic fields. Figure 26b shows the potential distributions for geometry F for applied fields of 0.03 and 0.12 Tesla. For the operating conditions shown, the potential at the lower field was approximately uniform with a magnitude of ~ 5 V. At the higher fields strengths, there was some structure, with a minimum on the centerline, and an overall increase of 3 to 5 volts. Increasing the discharge current did not have the same effect as increasing the field. Shown in Fig. 27 is the radial distribution of plasma potential at an axial distance of 20 cm from thruster geometry I for discharge currents of 1000 and 2000 A with no applied field. Increasing the discharge current to 2000 A clearly increased the centerline potential, decreased the data scatter, and did not affect the potentials measured at large radii. This contrasts to the results for increasing the applied field strength, which clearly caused a rapid rise in the plasma potential at large radii, and caused a potential minimum to appear on the thruster centerline. The decrease in scatter observed at higher discharge currents was due to the increase in density and associated increase in signal-to-noise ratio.

The anode geometry of the thruster had no measurable effect on the plasma-potential distribution at the axial distances of these measurements. However, the cathode geometry played a significant role in determining both the magnitude and behavior of the plasma potential. Shown in Fig. 28 is a comparison between the potential distributions 25 cm away from the thruster for geometries B and G, with B_z = 0.09 Tesla. The differences between them are clear, with the long cathode having a local maxima on the centerline and the short cathode having a global minima on the centerline. Comparing Fig. 28 with Fig. 25b it is

apparent that the minima in both distributions correspond with the highest temperature in the high-density plume. The axial potential distribution for the short cathode geometry is shown in Fig. 29, where it is seen that both the depth of the potential well and the rate of potential increase off axis decreased away from the thruster.

Discussion

These measurements clearly show that the applied field plays a dominant role in establishing the plume properties. The magnetic field strongly confines the plume, as evidenced by the great reduction in the rate at which the plasma density decreased in the axial direction and the steep radial density gradients observed with the applied field. In general, for the operating conditions and thruster geometries used in this study, the centerline electron density was between 3×10^{18} and 8×10^{18} m^{-3} and the temperature between 10,000 and 20,000 K. The centerline properties were relatively insensitive to operating condition so long as the applied field was on, though the imaging clearly showed an increase in excited ion state population with increasing applied field and discharge current. Thruster anode geometry did not have as large an impact on the plume properties as did the cathode length and shape. Large changes in plume structure were observed when the field was not present. The high-luminosity cone observed with the applied field appeared to come off the cathode surface and slowly diverge in the downstream direction. The plasma potential distribution was flat and only slightly positive without the applied field; however, with the applied-field there was a pronounced central minimum in the potential.

The effect of the applied field on the plume plasma can be qualitatively examined on the basis of three parameters: the electron Hall parameter, electron gyro radius, and ratio of the plasma thermal pressure to the magnetic pressure. These were calculated from

$$\Omega = \frac{eB_z}{m_e \nu_{e-i}} \; ; \quad r_e = \frac{m_e V}{eB_z} \; ; \quad \beta = \frac{\Sigma NkT}{B_z^2 / 2\mu_o} \qquad (3)$$

where the electron and ion temperatures and densities were assumed equal, and the mean electron velocity was set equal to the thermal speed based on the electron temperature. The electron - ion collision frequency was calculated from Spitzer's standard formulation[13]. At this point we have neglected the potential effects of plasma microturbulence, which would increase the effective collision rate and decrease the calculated Hall parameters. Values were calculated for the range of magnetic field strengths and electron densities measured in the plume. The results, presented in parametric form in Table 4, clearly show that the plasma was strongly confined by the magnetic field. Not only do the electrons gyrate many times around the field lines before undergoing a collision, but the gyro radii are much smaller than the observed density gradient length scales. In addition, the fact that the magnetic pressure was much greater than the plasma thermal pressure supports the observation of strong radial density gradients.

These estimates imply that the electrons in the plume moved predominantly along the field lines and do not move through regions with different properties. This result explains how the plume can support the sharply defined structure observed using the imaging. While this calculation appears to explain the presence of the lumosity cones, note that the electron density profiles show that the centerline density did not decrease axially, even though the magnetic-field lines were strongly diverging by an axial distance of 25 cm. This is shown in Fig. 30, where the vectors $\mathbf{B} = B_r\mathbf{r} + B_z\mathbf{z}$ are plotted, with the vector magnitude corresponding to the the magnetic-field magnitude. It is apparent that between axial distances of 25 and 35 cm, the field lines between radii of 5 and 10 cm are predominantly radial. While the plume does diverge in the axial direction, the apparent lack of a drop in centerline density indicates that the plasma is separating from the applied magnetic field lines. The apparent dichotomy between the calculated Hall parameters and the experimental evidence remains unresolved, though several authors have studied the phenomena of plasma/magnetic field separation[14,16].

It appears from the preceding discussion that as a result of applying the magnetic-field, electrons coming off the cathode surface will be partially confined to the region near the cathode. The corresponding reduction in radial electron flux would require an increase in the radial electric field to maintain current conduction at a constant level. Thus, not only would the plasma density near the cathode surface increase slightly, but the energy imparted by the fields to the particles would increase. The latter phenomena may be the source of the electron temperature structure observed with the long-cathode thrusters (Fig. 25b). In addition to the plume data, this argument is supported by observations made of the cathode surface during thruster operation with several applied-field strengths. It was found that the surface temperature of the cathode increased monotonically across the entire surface with applied-field strength. For a constant discharge current, this observation can only be accounted for by an increase in the ion-impingement current to the cathode. This result shows that the life and performance of applied-field thrusters with similar geometries may be fundamentally coupled. Performance measurements show a monotonic increase in efficiency and specific impulse with increasing applied-field, yet if this applied-field increases the cathode surface temperature it will certainly increase the material sublimation rate and may limit thruster life. While similar phenomena may occur in self-field MPD thrusters operated at the very high currents required to achieve magnetic fields of comparable magnitude to those applied in this study, the fundamental coupling of the discharge current to the magnetic-field strength in self-field thrusters will most likely preclude isolation of the physics controlling the phenomena.

The plasma potential measurements also support this proposed mechanism for cathode heating. It was found, Fig. 29, that increasing the applied field depressed the downstream centerline potential and increased the magnitude of the radial potential gradient. These measurements imply that the perpendicular electrical conductivity was strongly affected by the magnetic field. Generally speaking, the axial applied-field lines behave somewhat like equipotential lines, so that the centerline plume region is well connected, electrically, to the cathode tip, while at larger radii magnetic field lines that arise from the anode surface are well connected to the anode. The observation that the potential gradients decreased in the axial direction indicates the presence of radial currents in those regions.

Conclusions

Measurements of plume species, excited-state, electron-density, and temperature distributions show that the plumes of the applied-field MPD thrusters studied here were partially ionized, with centerline electron densities and temperatures ranging from 2×10^{18} to 8×10^{18} m^{-3} and from 7,500 to 20,000 K, respectively. Both these magnitudes and the plume structure were very sensitive to the presence of the applied field, which was found to strongly confine the plume plasma. For the operating conditions studied here, the degree of confinement, as indicated by radial density gradients, increased monotonically with applied-field strength, though the centerline densities did not show a commensurate increase. While calculations of the electron Hall parameter indicate that the plasma is strongly coupled to the applied magnetic field lines, the density distributions show that the plasma does not follow magnetic flux tubes in the downstream region, implying that the plume does separate from the applied magnetic field.

Measurements of the plasma-potential distributions confirmed the strong influence of the applied field, which appeared to subtantially reduce the electrical conductivity perpendicular to the magnetic field. This phenomenon not only resulted in increased radial potential gradients, but also increased the cathode surface temperature. The latter phenomenon may fundamentally couple the performance and life of applied-field thrusters of similar geometry.

Acknowledgements

The authors wish to thank John Naglowsky, Larry Schultz, John Eckert, Tom Ralys, David Wolford, John McAlea, Rob Butler, John Miller, Gerry Schneider and Cliff Schroeder for their invaluable support on this project. Thanks also go to Dr. Michael LaPointe for use of his magnetic field calculation code.

References

1. Sovey, J. and Mantenieks, M., "Performance and Lifetime Assessment of MPD Arc Thruster Technology," Journal of Propulsion and Power, Vol. 7, No. 1, Jan.-Feb. 1991, pp. 71-83.
2. Tahara, H., Yasui, H., Kagaya, Y., and Yoshikawa, T., "Development of a Quasi-Steady MPD Arcjet Thruster for Near-Earth Missions," AIAA Paper 87-1001, May 1987.
3. Kagaya, Y., Yoshikawa, T., and Tahara, H., "Quasi-Steady MPD Arcjets with Applied Magnetic Fields," AIAA Paper 85-2001, Oct. 1985.
4. Myers, R.M., "Applied Field MPD Thruster Geometry Effects," AIAA Paper 91-2342, June 1991.
5. Mantenieks, M.A., Sovey, J.S., Myers, R.M., Haag, T.W., Raitano, P., and Parkes, J.E., "Performance of a 100 kW Class Applied Field MPD Thruster," AIAA Paper 89-2710,

July 1989, see also NASA TM 102312, July, 1989.
6. Haag, T., "Design of a Thrust Stand for High Power Electric Propulsion Devices," AIAA Paper 89-2829, July 1989, see also NASA TM 102372, July, 1989.
7. Sudharsanan, S.I., "The Abel Inversion of Noisy Data Using Discrete Integral Transforms," M.S. Thesis, The University of Tennessee, Knoxville, August 1986.
8. Cremers, C. and Birkebak, R.C., "Application of the Abel Integral Equation to Spectrographic Data," Applied Optics, Vol. 5, No. 6, June 1966, pp. 1057-1064.
9. Chung, P. M., Talbot, L., and Touryan, K.J. "Electric Probes in Stationary and Flowing Plasmas: Part 1. Collisionless and Transitional Probes," and, "Part 2. Continuum Probes," AIAA Journal, Vol. 12, No. 2, Feb. 1974, pp. 133 - 154.
10. Swift, J.D., and Schwar, M.J., "Electric Probes for Plasma Diagnostics," American Elsevier Publishing Co., Inc., 1970.
11. Wiese, W.L, Smith, M.W. and Miles, B.M., "Atomic Transition Probabilities, Vol. II, Sodium Through Calcium," National Stand. Ref. Data Series, National Bureau of Standards, Vol. 22, Oct. 1969.
12. Myers, R.M., "Plume Characteristics of MPD Thrusters: A Preliminary Examination," AIAA Paper 89-2832, July 1989, see also NASA CR 185130, Sept. 1989.
13. Spitzer, L., "Physics of Fully Ionized Plasmas," Interscience Publishers, Inc., New York, 1956.
14. Kosmahl, H.G., "Three-Dimensional Plasma Acceleration through Axisymmetric Diverging Magnetic Fields based on Dipole Moment Approximation," NASA TN D-3782, Jan. 1967.
15. Walker, E. and Seikel, G., "Axisymmetric Expansion of a Plasma in a Magnetic Nozzle including Thermal Conduction," NASA TN D-6154, Feb. 1971.
16. Hooper, E. B., "Plasma Detachment from a Magnetic Field," AIAA Paper 91-2590, June 1991.

Geometry	Anode Radius R_a, cm	Anode Length L_a, cm	Cathode Radius R_c, cm	Cathode Length L_c, cm
A	2.5	7.6	0.64	7.6
B	3.81	7.6	0.64	7.6
C	5.1	7.6	0.64	7.6
E	5.1	7.6	1.27	7.6
F	5.1	15.2	1.27	7.6
G	3.81	7.6	0.64	2.5 (conical)
I	3.81	7.6	3.0 OD, 1.0 ID (Hollow)	6.1

Table 1: Dimensions of MPD thrusters used in this study

Plasma Species	Identified lines, nm
ArI	404.6, 419.8, 433.4, 436.4, 696.5
ArII	355.9, 358.8, 407.2, 433.2, 487.9
HI	486.1
WI	368.2, 368.4, 368.8
CuII	491.8, 490.7

Table 2: Plasma species and the most prominent lines identified

Wavelength (nm)	E_u (eV)	G_u	$A_{ik} \times 10^8$ (sec^{-1})
410.3	22.76	4	1.3
408.2	19.73	6	0.027
407.2	21.56	6	0.57
405.3	23.86	4	1.50
404.3	21.55	4	1.40

Table 3. Spectral lines and constants used to determine electron temperature.

B_z, Tesla	$N_e + N_i$ (m^{-3})	Electron Hall Parameter	Electron gyro radius (cm)	Thermal P / Magnetic P
.02	5×10^{17}	176	1.76×10^{-2}	4.33×10^{-4}
.02	1×10^{18}	88	"	8.7×10^{-4}
.02	5×10^{18}	18	"	4.33×10^{-4}
.02	1×10^{19}	9	"	8.7×10^{-3}
.05	5×10^{17}	439	7.1×10^{-3}	7×10^{-5}
.05	1×10^{18}	220	"	1.4×10^{-4}
.05	5×10^{18}	44	"	7×10^{-4}
.05	1×10^{19}	22	"	1.4×10^{-3}
.1	5×10^{17}	878	3.5×10^{-3}	1.7×10^{-5}
.1	1×10^{18}	439	"	3.5×10^{-5}
.1	5×10^{18}	88	"	1.7×10^{-4}
.1	1×10^{19}	44	"	3.5×10^{-4}

Table 4. Electron Hall Parameter, gyro radius and ratio of thermal to magnetic pressures for $T_e = T_i = 10^4$ K and densities/magnetic fields observed in this work.

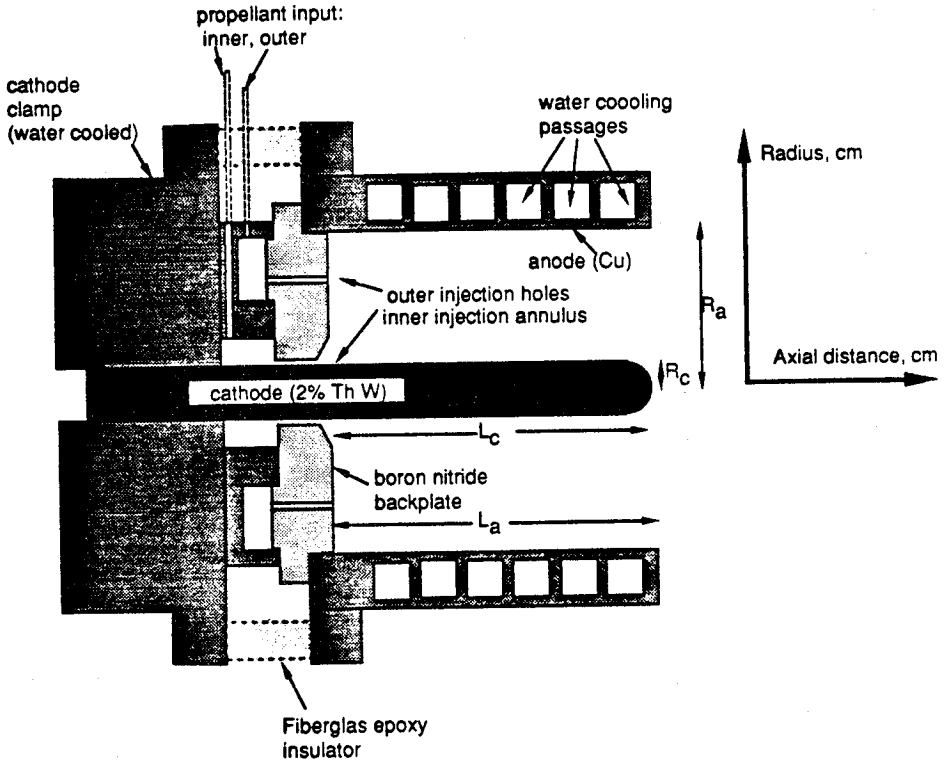

Figure 1. MPD thruster schematic showing coordinate system used for plume measurements. Applied field magnet not shown. Electrode dimensions are given in Table 1.

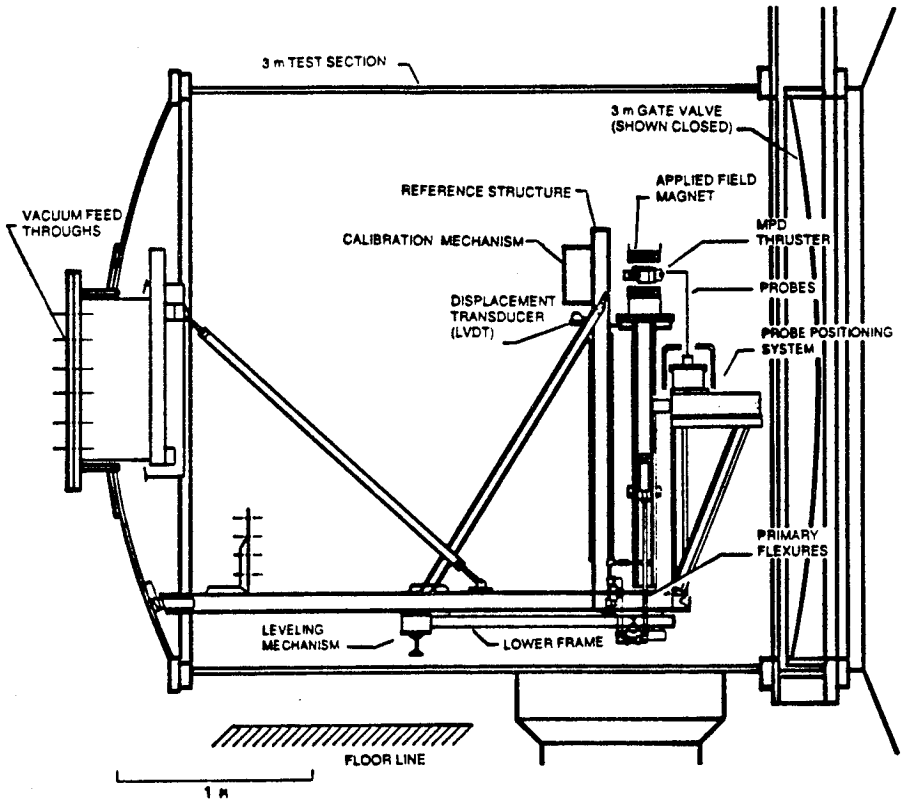

Figure 2. Schematic of MPD thruster test facility showing thrust stand and probe positioning system.

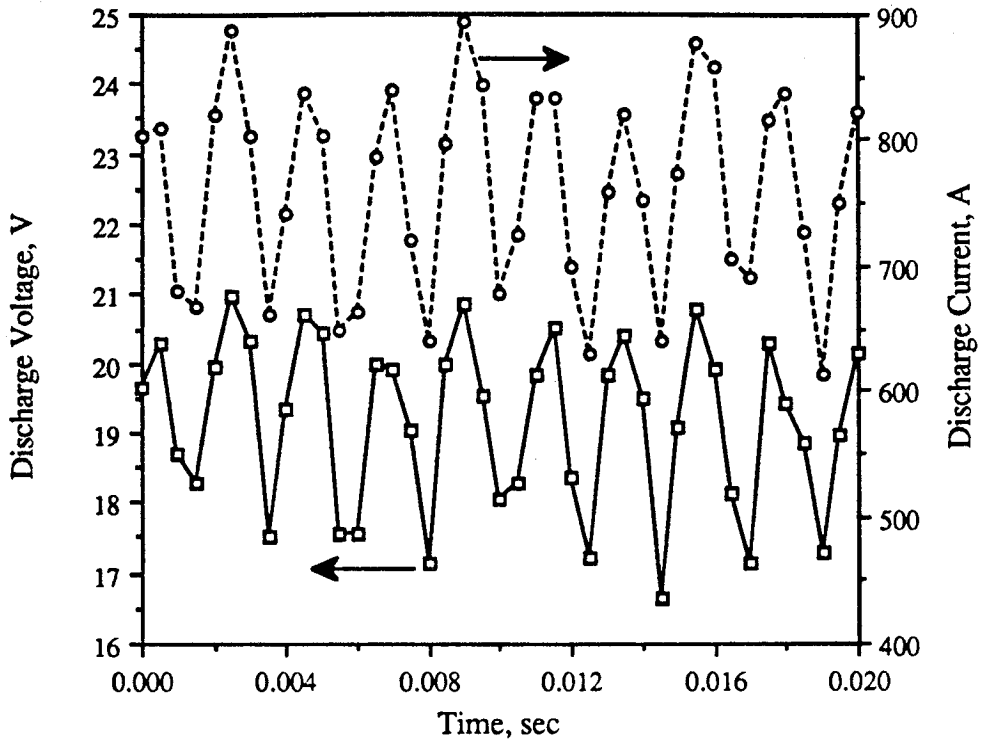

Figure 3. Thruster current and voltage ripples for geometry I. J_d = 750 A, Bz = 0 T, 0.1 g/s argon mass flow.

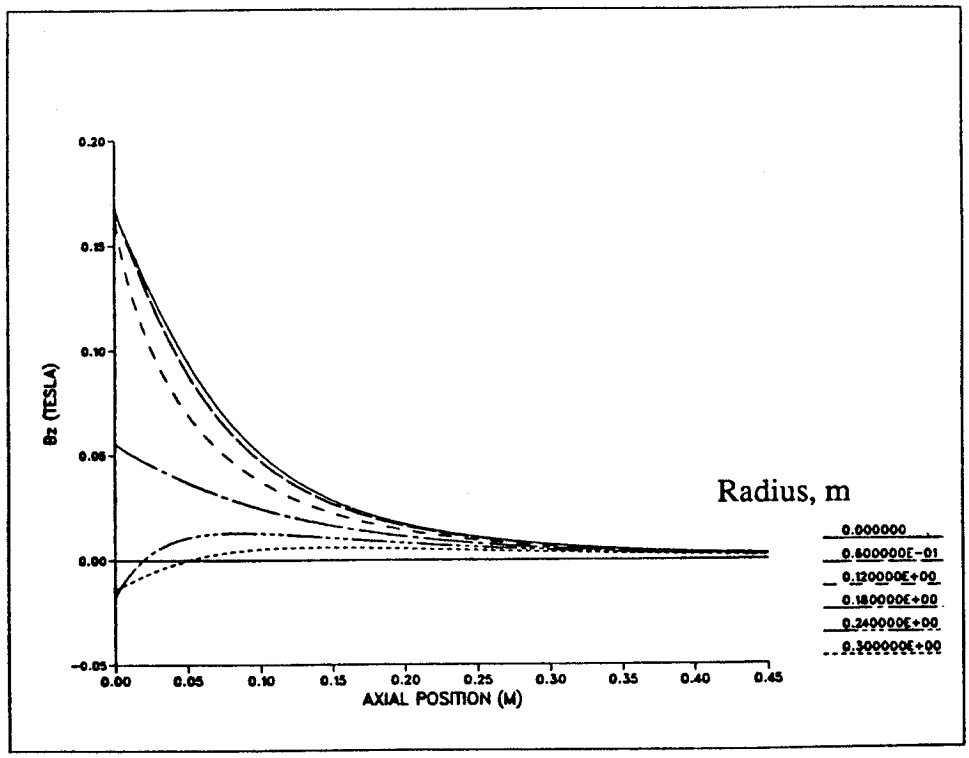

Figure 4. Axial magnetic field strengths as a function of axial distance for the 15.3 cm I.D. magnet with 1400 A. The origin is at the centerline of the magnet exit plane.

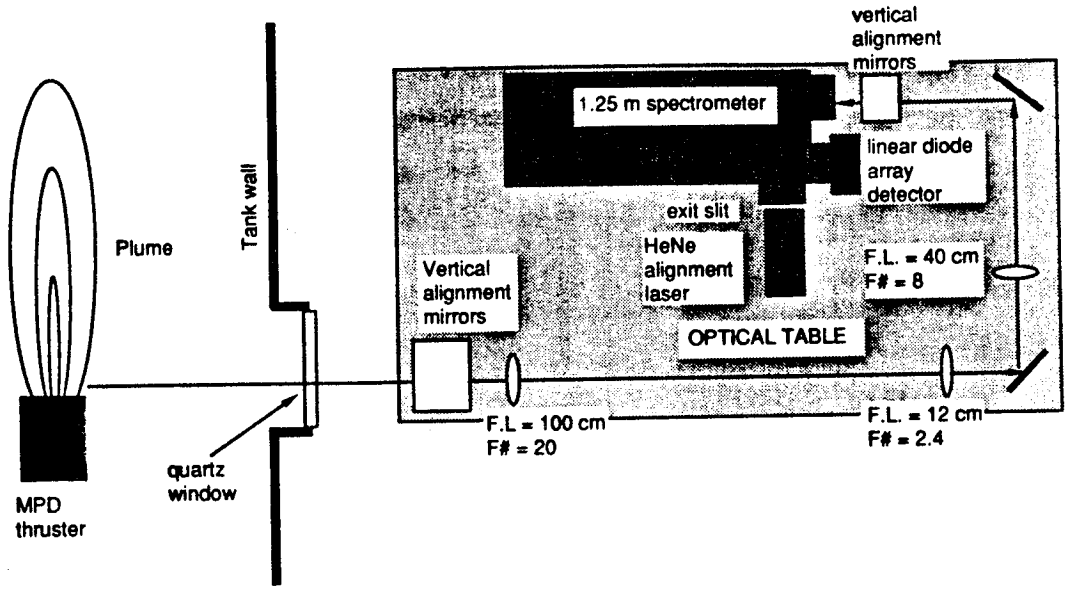

Figure 5. Optical path for emission spectroscopy measurements.

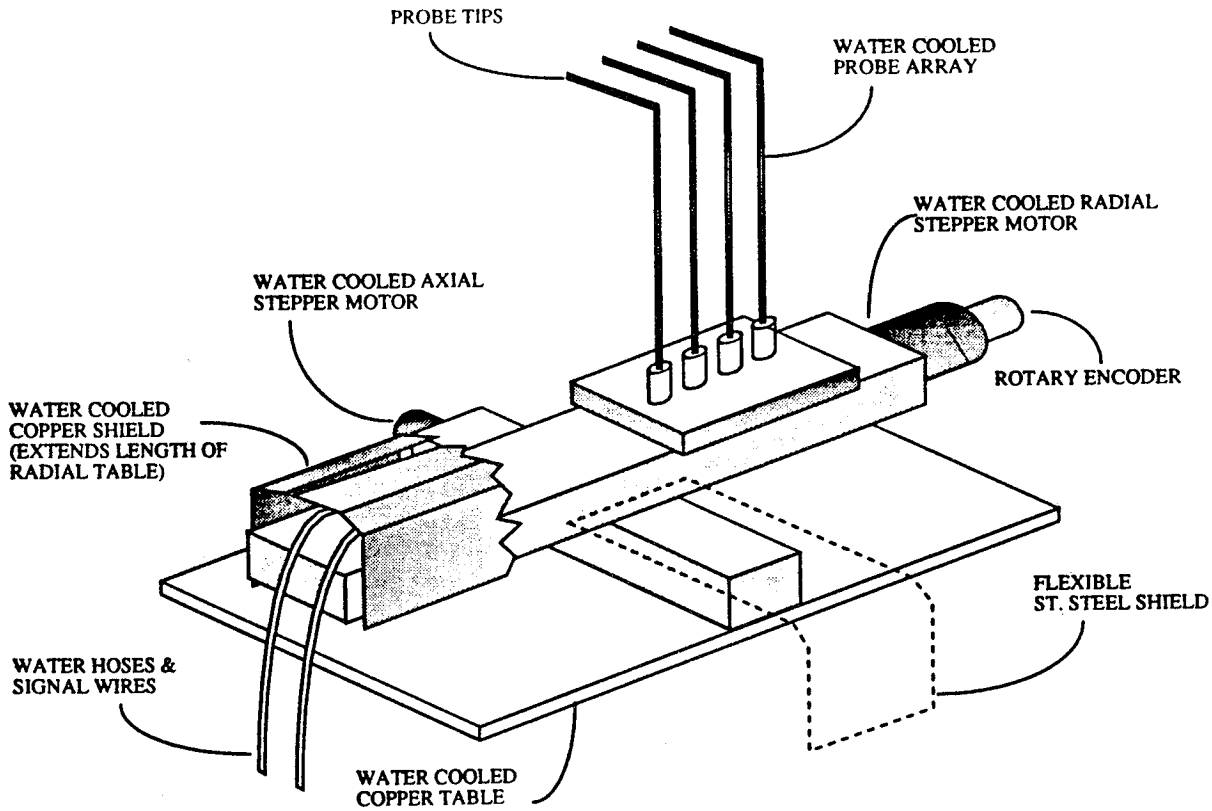

Figure 6. Schematic of probe positioning system showing axial and radial tables with 4 probes mounted on the radial table.

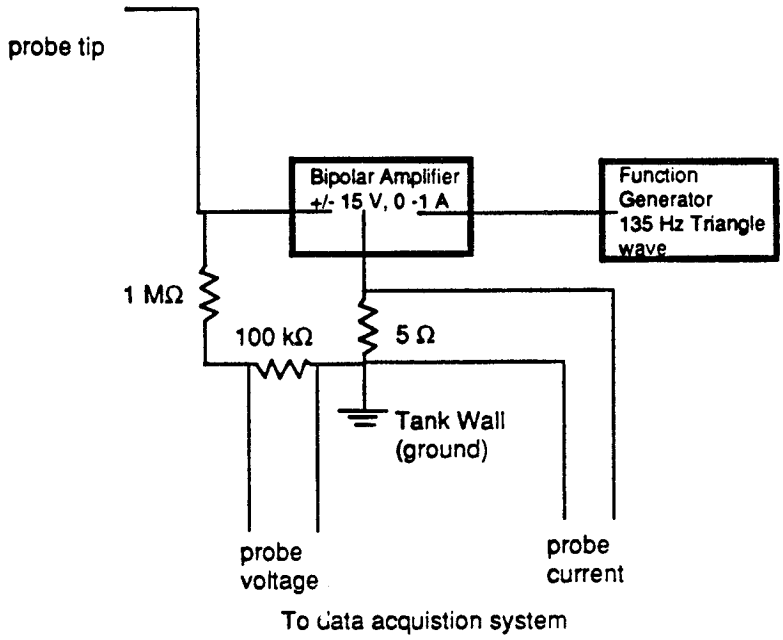

Figure 7. Electric probe circuit used for electron temperature and density measurements.

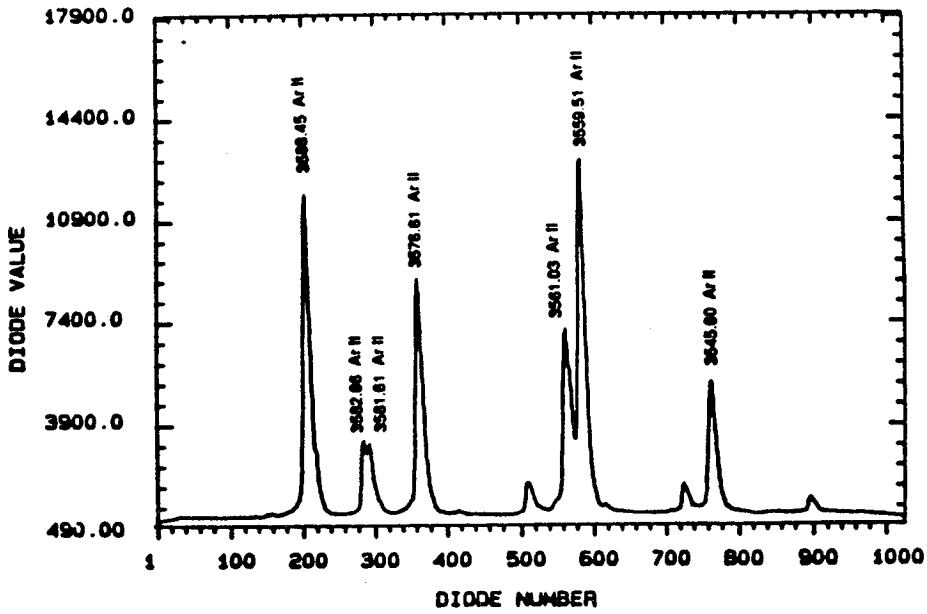

Figure 8. Spectrum centered at 356 nm with a bandpass of 8.19 nm.

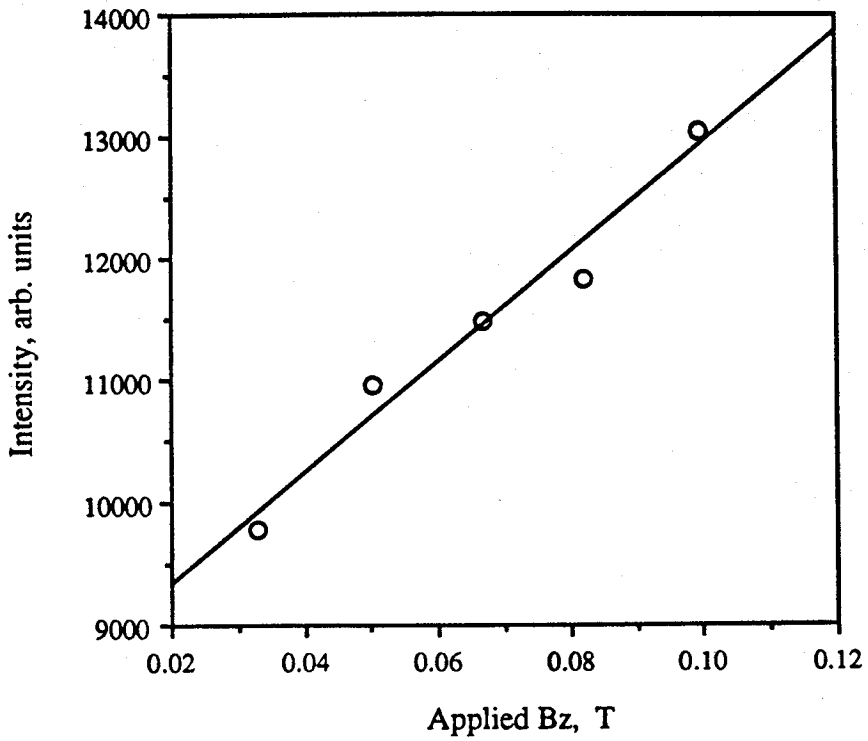

Figure 9. Peak centerline intensity as a function of applied field strength for geometry A. J_d = 750 A, 0.035 g/s hydrogen propellant.

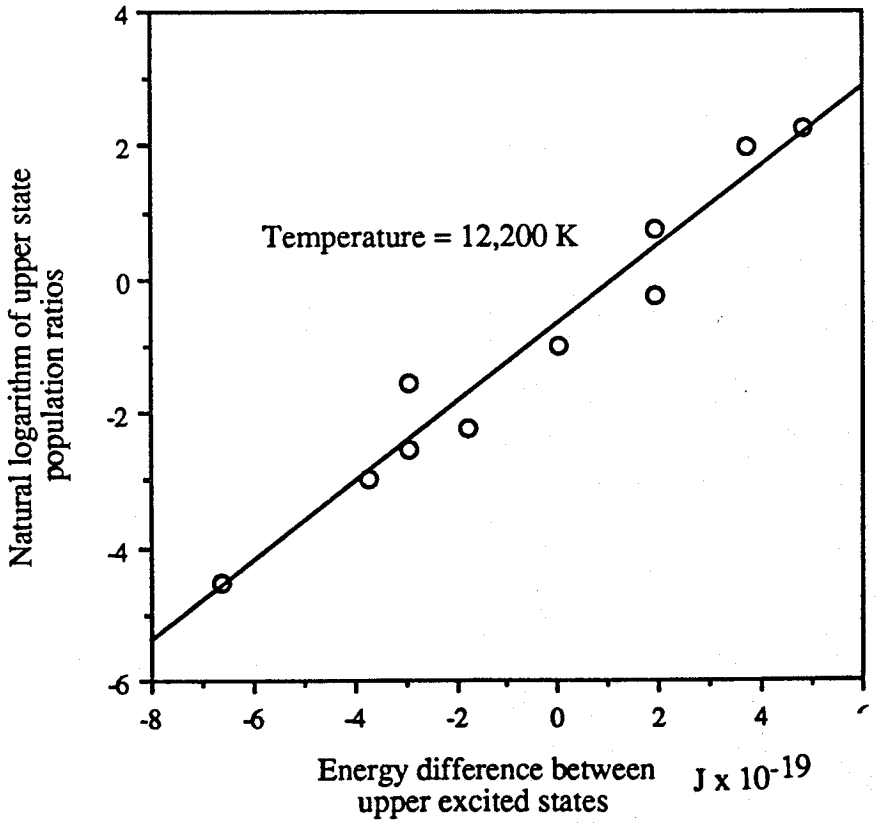

Figure 10. Boltzmann plot for line-of-sight intensities 5 mm in front of thruster geometry C. J_d = 1000 A, B_z = 0.051 T, 0.1 g/s argon flow rate.

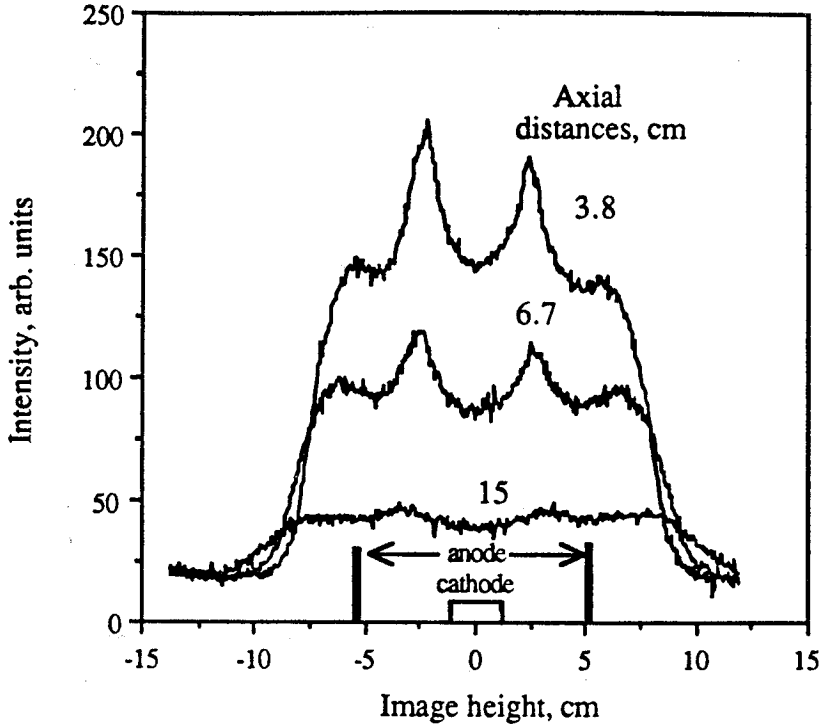

Figure 11. Raw image intensity profiles taken with the 488 nm filter using thruster geometry E. J_d = 1250 A, B_z = 0.042 T, 0.1 g/s argon flow rate.

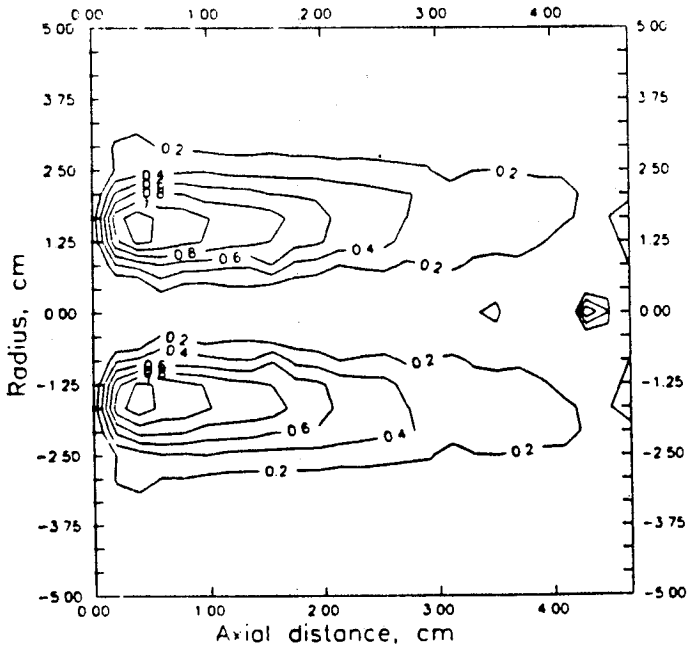

a. B_z = 0.026 T
Contour interval = 0.2

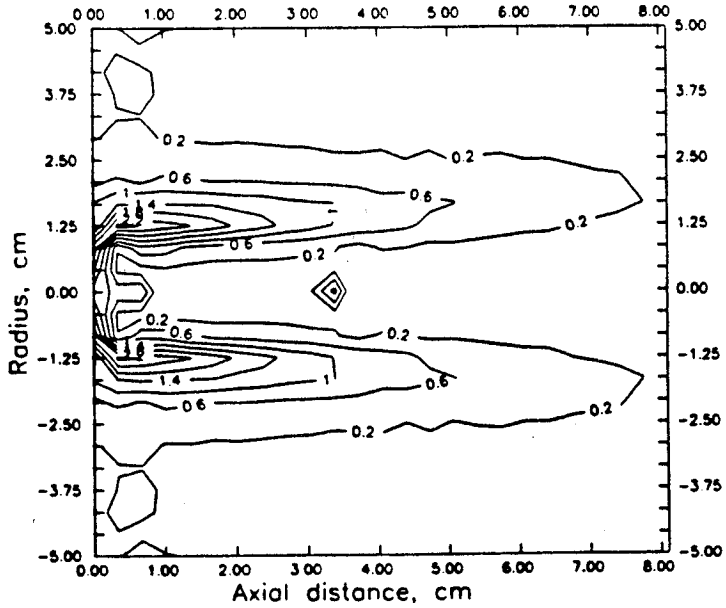

b. B_z = 0.064 T
Contour interval = 0.4

Figure 12. Contour plots of relative emission coefficient for the 514.7 nm transition using thruster geometry C. J_d = 1000 A, 0.1 g/s argon flow rate.

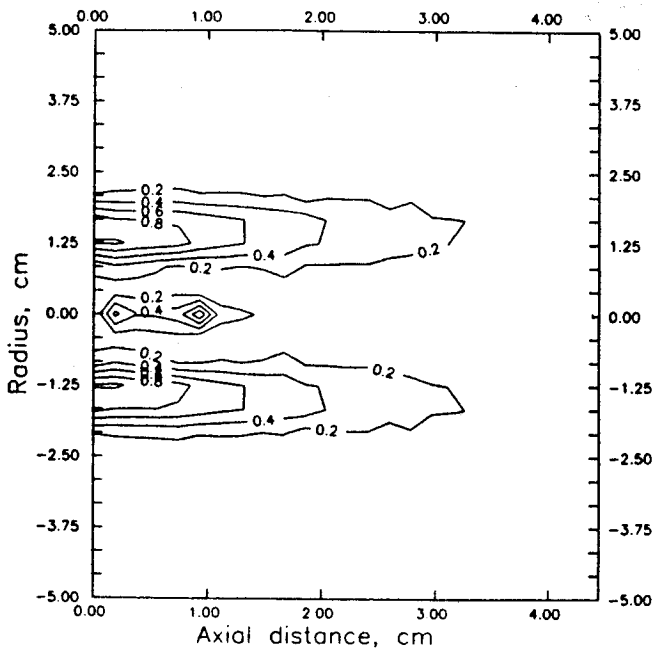

a. $J_d = 750$ A

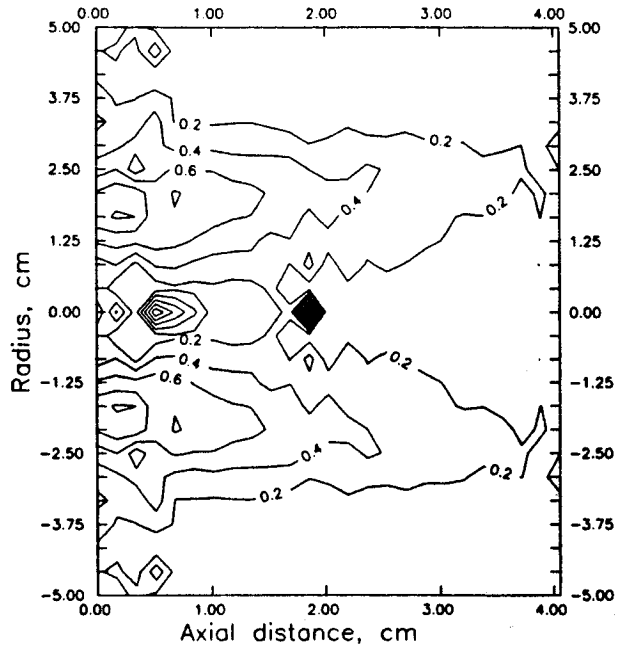

b. $J_d = 1500$ A

Figure 13. Contour plots of relative emission coefficient for the 514.7 nm transition using thruster geometry C. Two discharge currents, $B_z = 0.034$ T, 0.1 g/s argon flow. rate. Contour interval = 0.2.

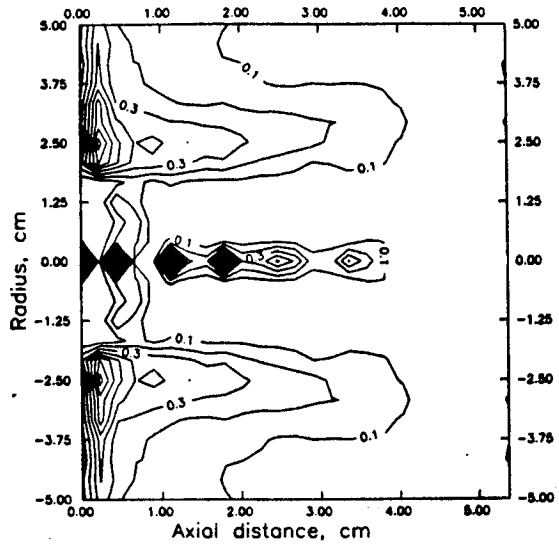

Figure 14. Contour plot of relative emission coefficient for the 487.9 nm transition using for thruster geometry E. J_d = 1250 A, B_z = 0.030 T, 0.1 g/s argon flow rate.

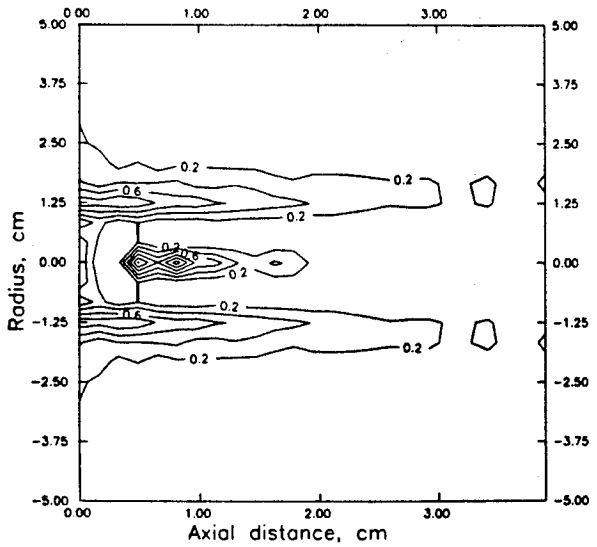

a. 7.6 cm long, hemispherical tipped cathode.

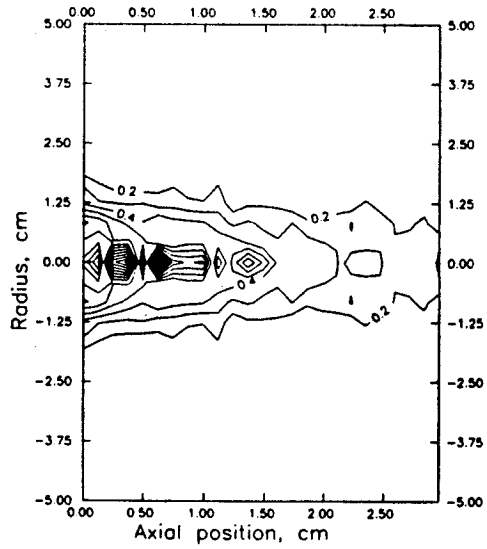

b. 2.5 cm long, conical tipped cathode.

Figure 15. Contour plots of relative emission coefficient for the 514.7 nm transition with a 3.8 cm radius anode. J_d = 1000 A, B_z = 0.116 T, 0.1 g/s argon flow rate.

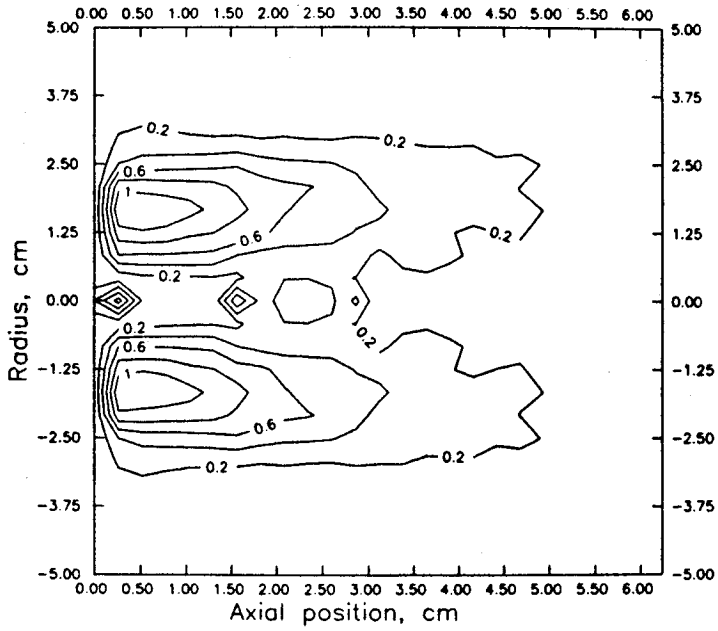

a. 5.2 mg/s hydrogen

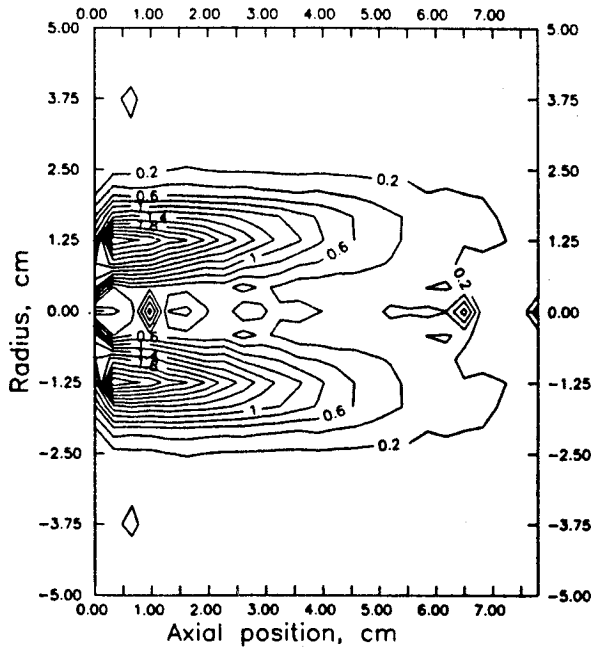

b. 17.0 = mg/s hydrogen

Figure 16. Effect of hydrogen addition on the relative emission coefficients for the 487.9 nm transition using geometry C. J_d = 1000 A, B_z = 0.034 T, 0.1 g/s argon flow rate. Contour interval = 0.2.

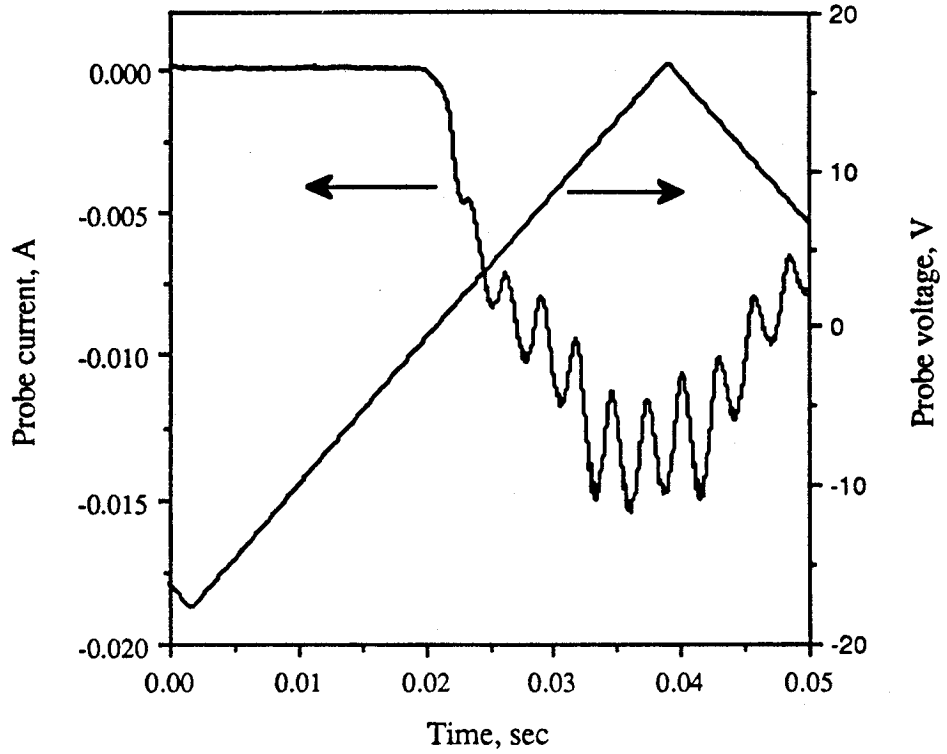

Figure 17. Raw electric probe voltage and current signals taken with thruster geometry I outside the main plume. J_d = 750 A, B_z = 0 T, 27 voltage ramps/sec.

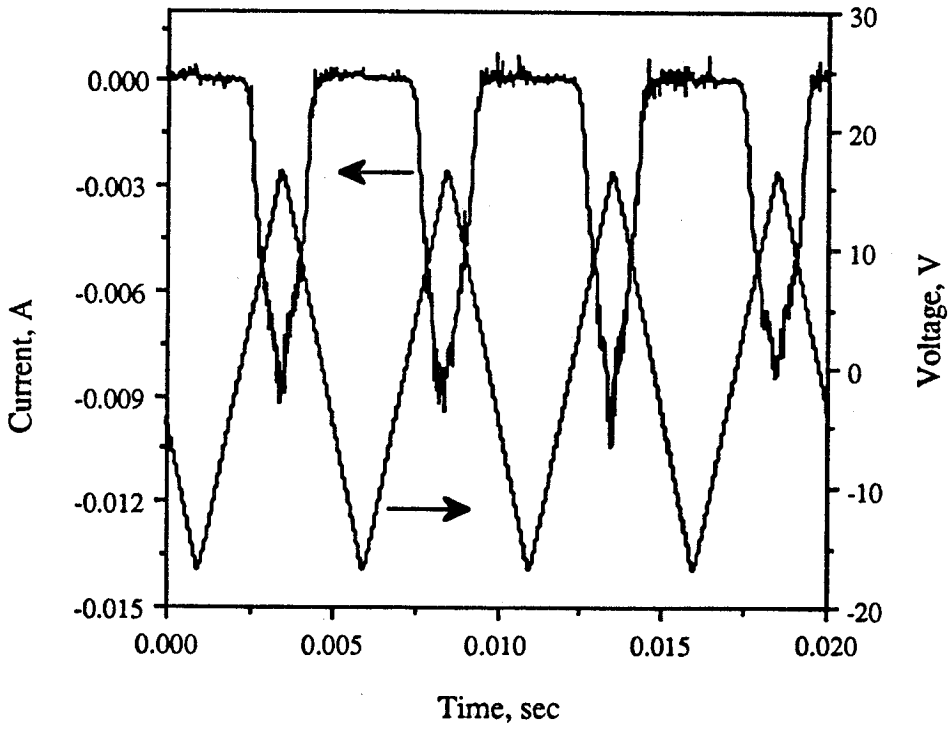

Figure 18. Electric probe current and voltage traces taken with thruster geometry F outside the main plume. J_d = 1250 A, B_z = 0.038 T, 270 voltage ramps/sec.

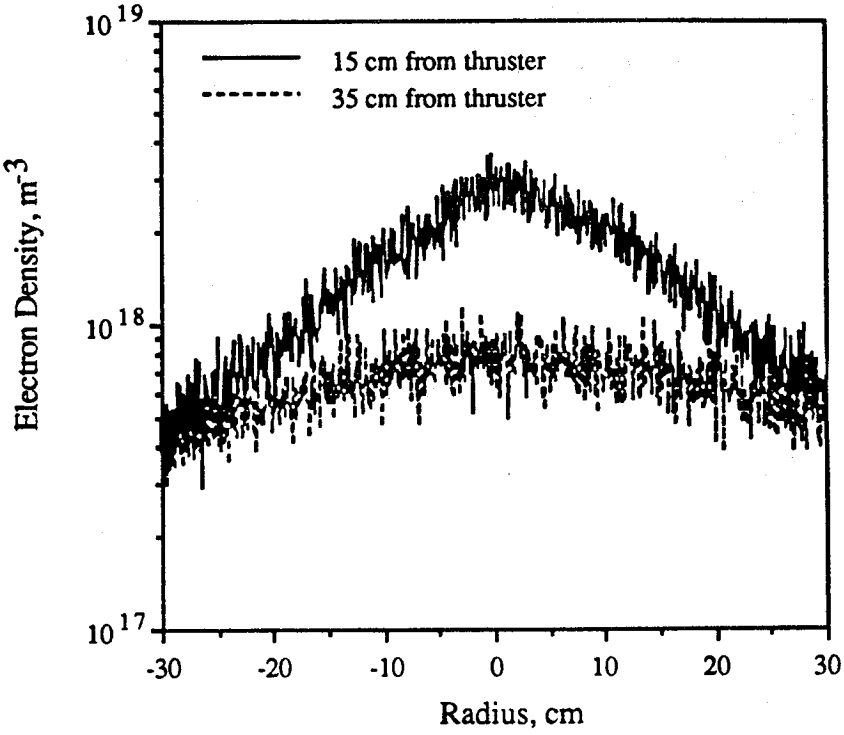

a. $B_Z = 0$ T

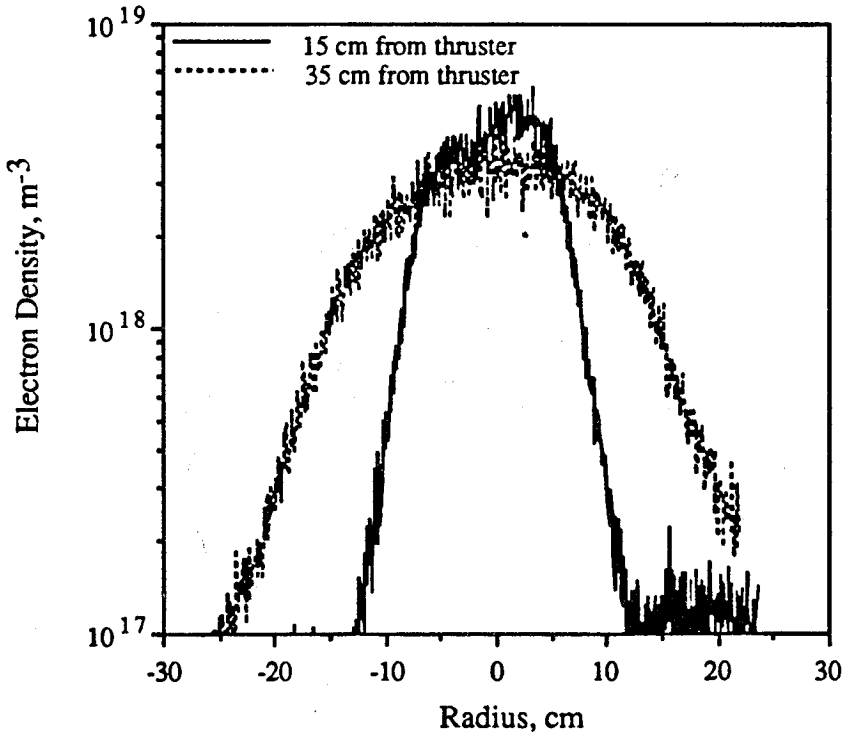

b. $B_Z = 0.10$ T

Figure 19. Electron density profiles 15 and 35 cm from thruster geometry I with and without an applied field. J_d = 1000 A, 0.15 g/s argon flow rate.

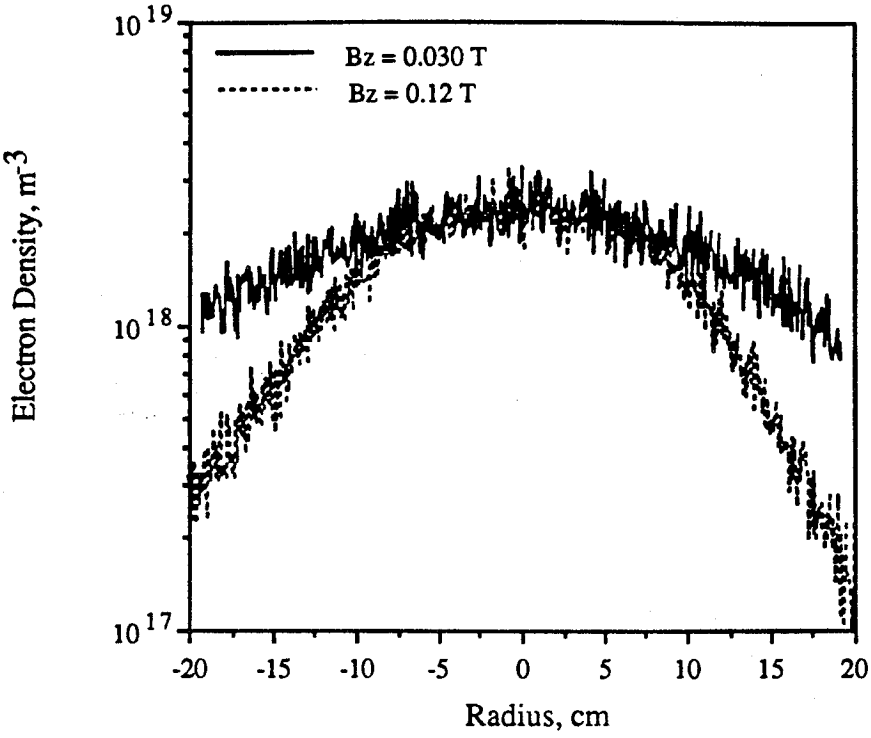

Figure 20. Electron density profiles 35 cm from thruster geometry F. Two magnetic field strengths, J_d = 1000 A, 0.1 g/s argon.

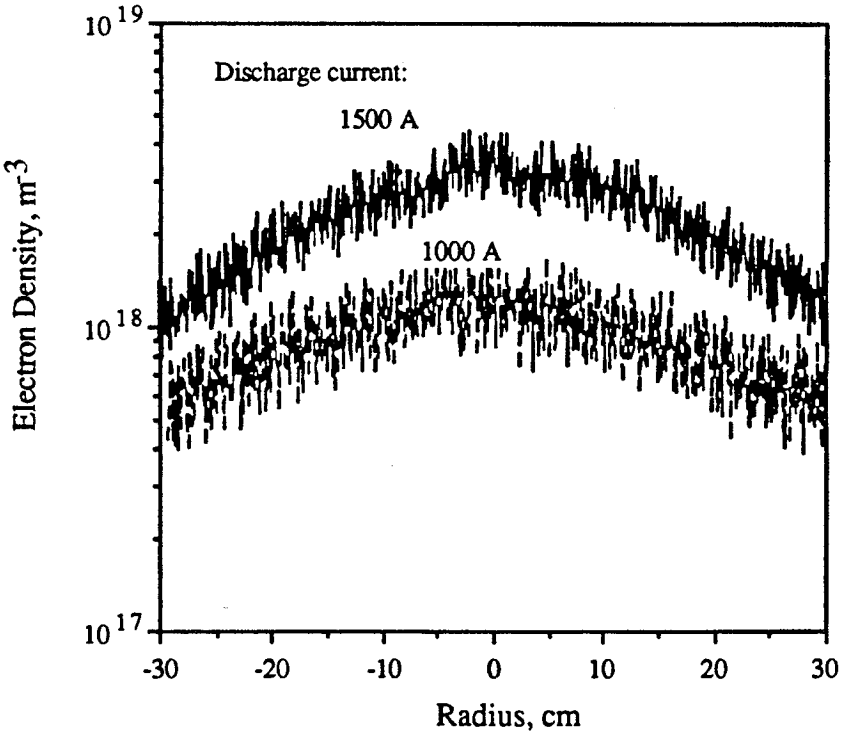

Figure 21. Electron density profiles 25 cm from thruster geometry I. Two discharge currents, B_Z = 0 T, 0.15 g/s argon flow rate.

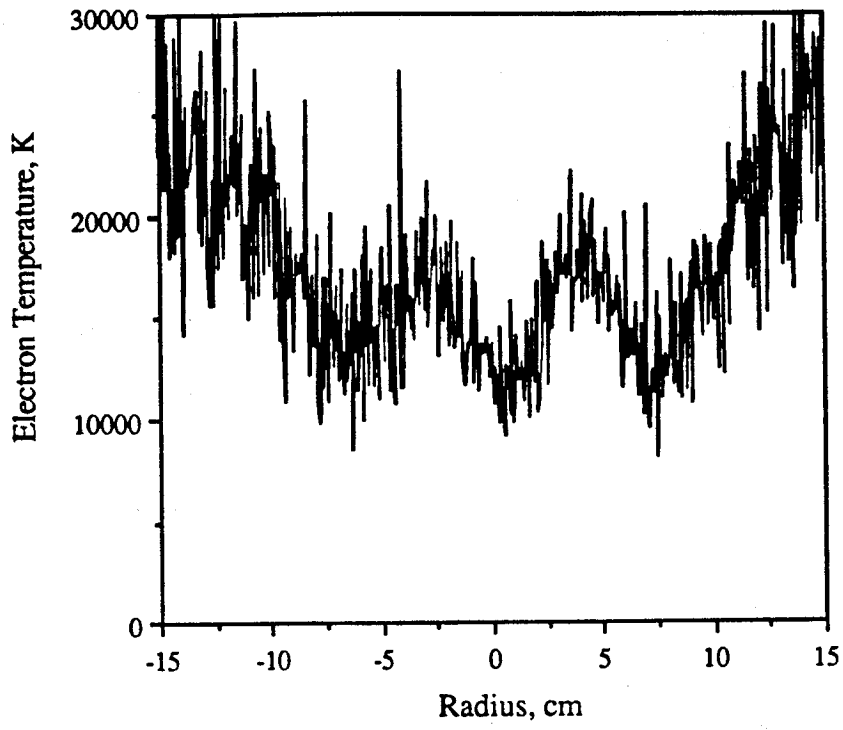

Figure 22. Electron temperature profile 25 cm away from thruster geometry B. J_d = 1000 A, B_z = 0.1 T, 0,1 g/s argon flow rate.

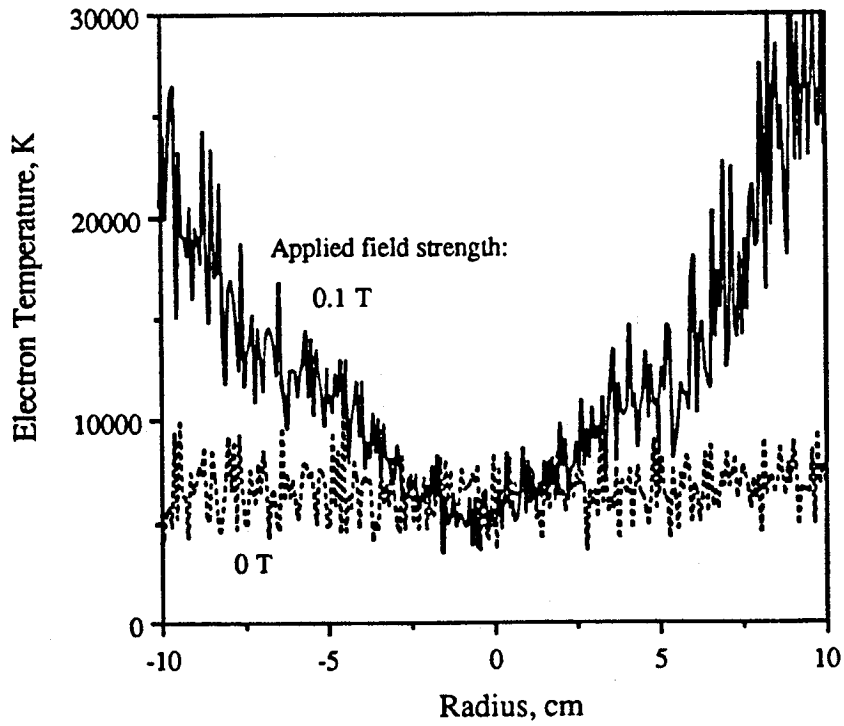

Figure 23. Electron temperature distributions 15 cm away from thruster geometry I. Two values of applied field strength, J_d = 1000 A, 0.15 g/s argon flow rate.

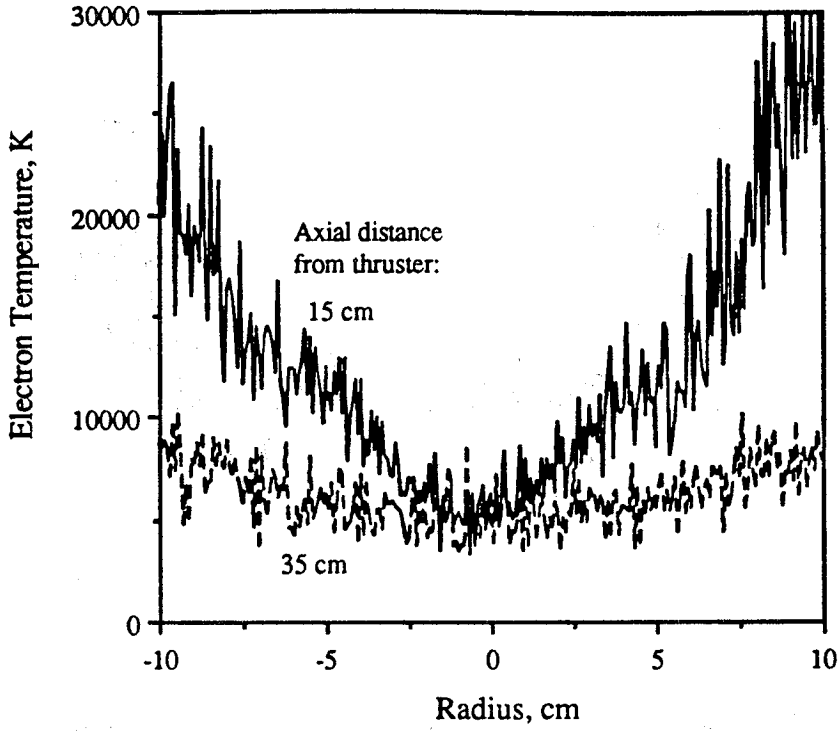

Figure 24. Electron temperature distribution for thruster geometry I. J_d = 750 A, B_z = 0.1 T, 0.1 g/s argon flow rate.

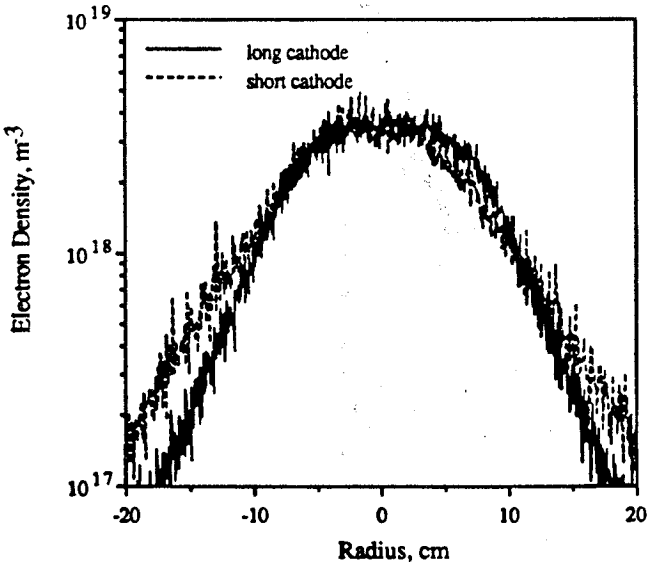

a. Electron densities.

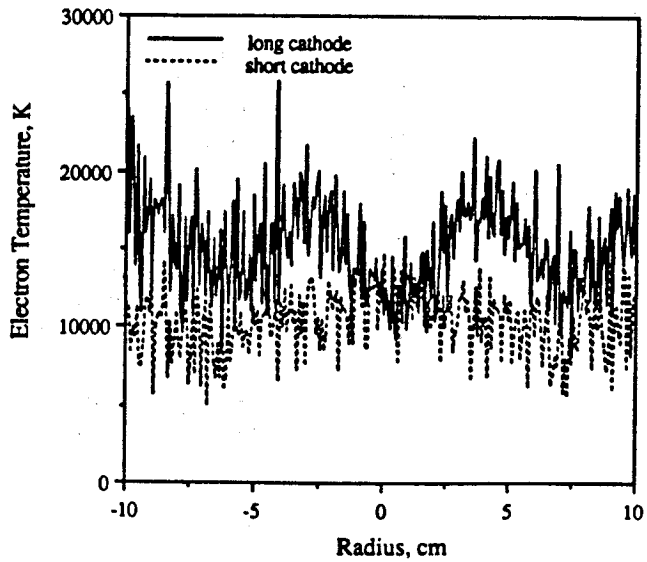

b. Electron temperatures.

Figure 25. Electron density and temperature profiles 25 cm away from thruster geometries B and G. J_d = 1000 A, B_z = 0.091 T, 0.1 g/s argon flow rate.

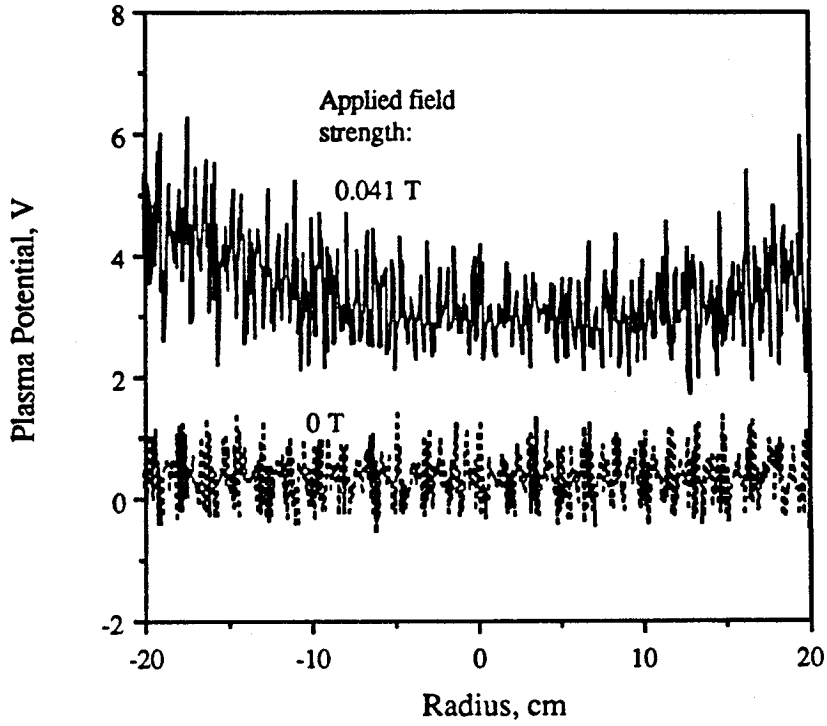

a. Geometry I, 0.15 g/s argon flow rate.

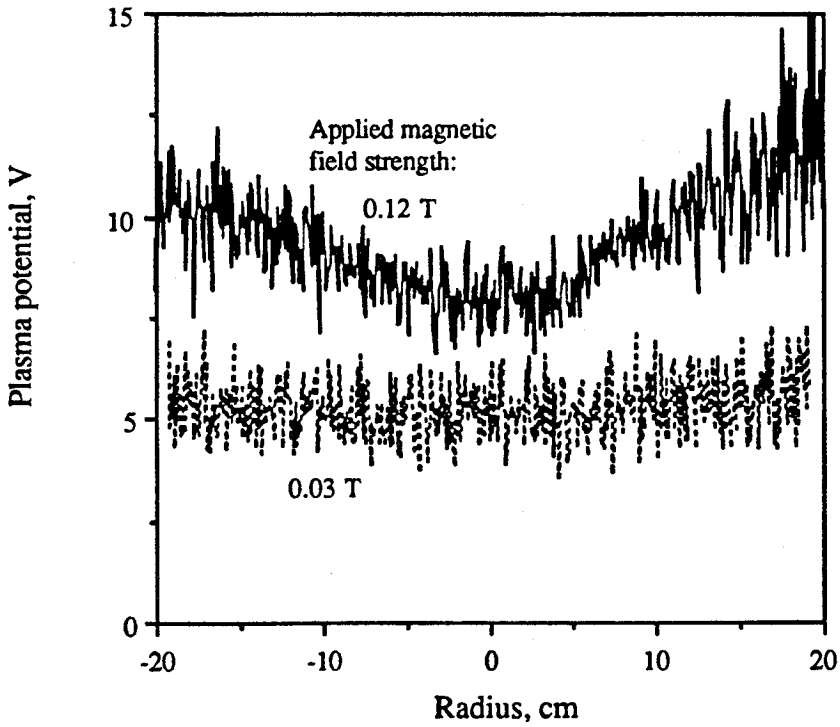

b. Geometry F, 0.1 g/s argon flow rate.

Figure 26. Plasma potential profiles for thruster geometries I and F for a discharge current of 1000 A and two applied field strengths each.

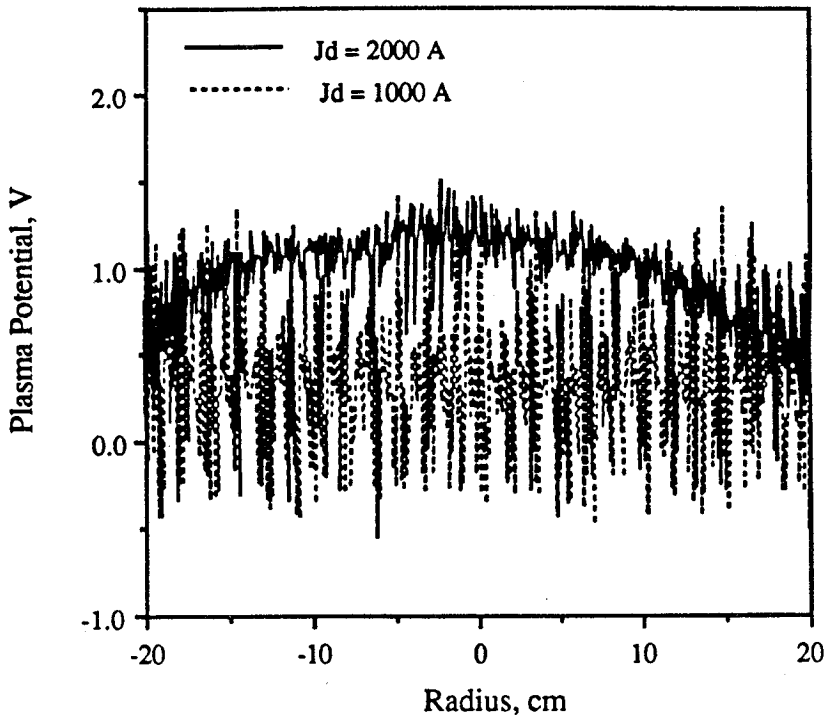

Figure 27. Plasma potential profiles 25 cm from thruster geometry I. Two discharge currents, B_z = 0 T, 0.15 g/s argon flow rate.

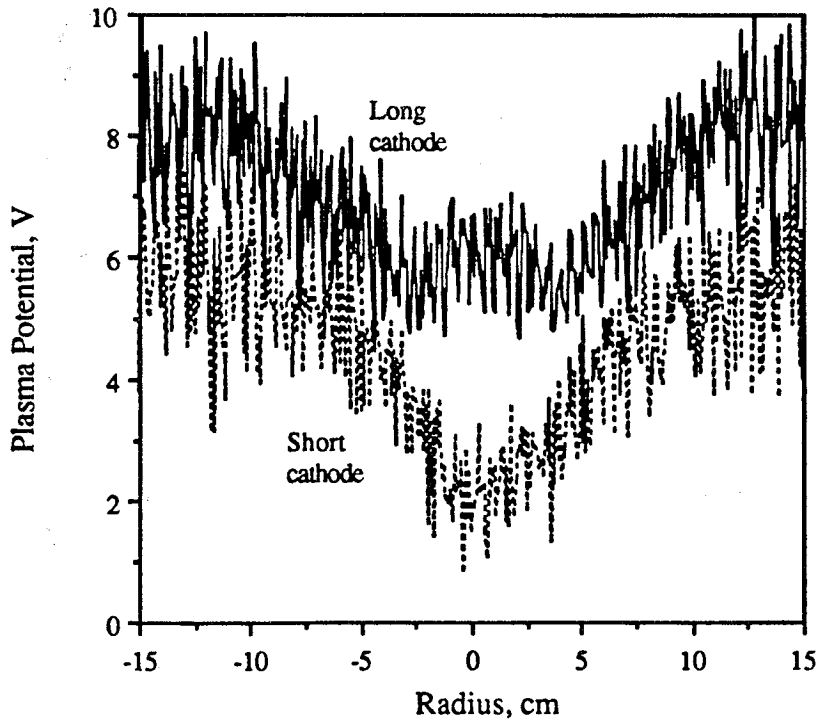

Figure 28. Plasma potential profiles 25 cm from thruster geometries B and G. J_d = 1000 A, B_z = 0.091 T, 0.1 g/s argon flow rate.

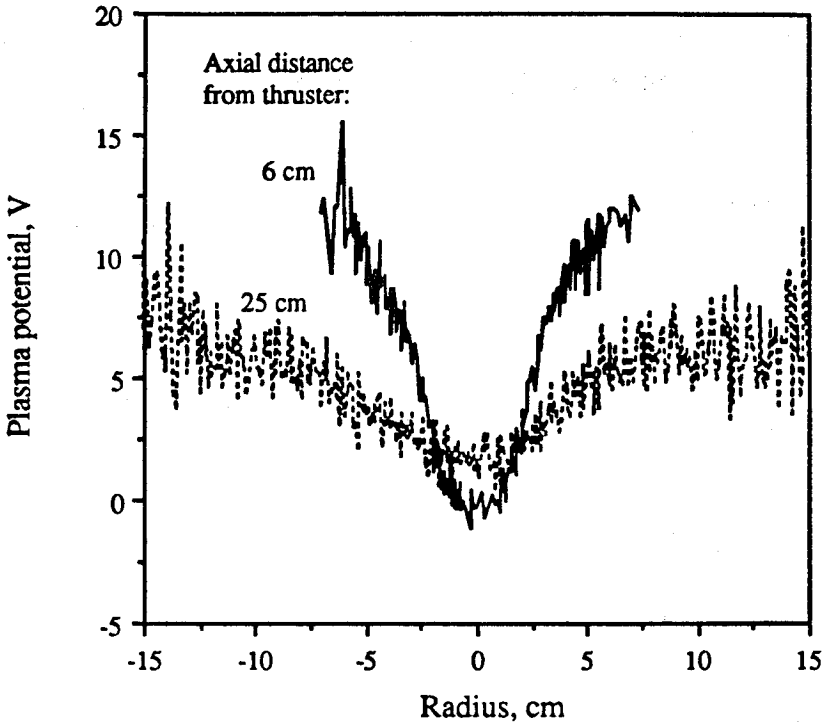

Figure 29. Plasma potential distributions 6 and 25 cm from thruster geometry G. J_d = 750 A, B_z = 0.13 T, 0.1 g/s argon flow rate.

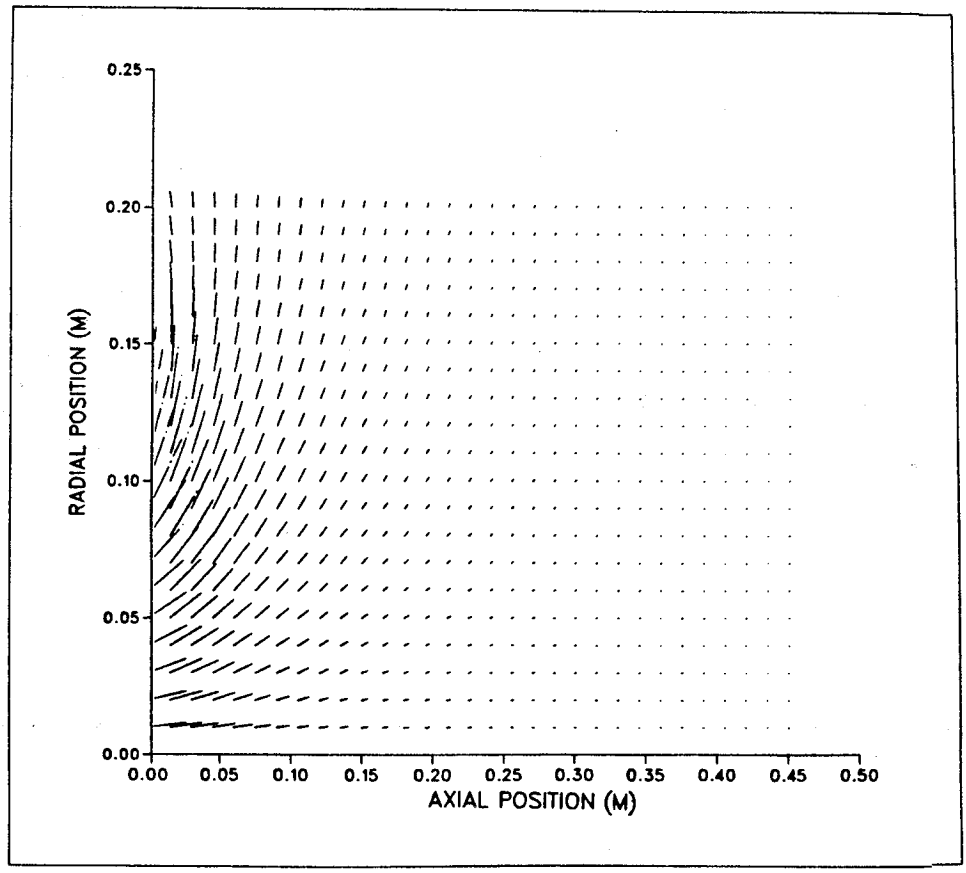

Figure 30. Magnetic field vectors for 15.3 cm I.D. magnet with a coil current of 1400 A. Vector lengths are proportional to field stregths. Origin is at centerline of magnet exit plane.

NASA
National Aeronautics and Space Administration

Report Documentation Page

1. Report No.	2. Government Accession No.	3. Recipient's Catalog No.
NASA CR-187165 AIAA-91-2339		

4. Title and Subtitle
A Preliminary Characterization of Applied-Field MPD Thruster Plumes

5. Report Date
August 1991

6. Performing Organization Code

7. Author(s)
Roger M. Myers, David Wehrle, Mark Vernyi, James Biaglow, and Shawn Reese

8. Performing Organization Report No.
None (E-6426)

10. Work Unit No.
506-42-31

9. Performing Organization Name and Address
Sverdrup Technology, Inc.
Lewis Research Center Group
2001 Aerospace Parkway
Brook Park, Ohio 44142

11. Contract or Grant No.
NAS3-25266

13. Type of Report and Period Covered
Contractor Report
Final

12. Sponsoring Agency Name and Address
National Aeronautics and Space Administration
Lewis Research Center
Cleveland, Ohio 44135-3191

14. Sponsoring Agency Code

15. Supplementary Notes
Project Manager, James Sovey, Space Propulsion Technology Division, NASA Lewis Research Center. Prepared for the 27th Joint Propulsion Conference cosponsored by AIAA, SAE, ASME, and ASEE, Sacramento, California, June 24-27, 1991. Roger M. Myers, Sverdrup Technology, Inc.; David Wehrle, Cleveland State University, Cleveland, Ohio 44115; Mark Vernyi, University of Akron, Akron, Ohio 44325; James Biaglow, University of Cincinnati, Cincinnati, Ohio 45221; Shawn Reese, Ohio University, Athens, Ohio 45701. Responsible person, Roger M. Myers, (216) 433-8548.

16. Abstract
Electric probes, quantitative imaging, and emission spectroscopy were used to study the plume characteristics of applied-field MPD thrusters. The measurements showed that the applied magnetic field plays the dominant role in establishing the plume structure, followed in importance by the cathode geometry and propellant. The anode radius had no measurable impact on the plume characteristics. For all cases studied the plume was highly ionized, though spectral lines of neutral species were always present. Centerline electron densities and temperatures ranged from 2×10^{18} to 8×10^{18} m^{-3} and from 7500 to 20,000 K, respectively. The plume was strongly confined by the magnetic field, with radial density gradients increasing monotonically with applied field strength. Plasma potential measurements show a strong effect of the magnetic field on the electrical conductivity and indicate the presence of radial current conduction in the plume.

17. Key Words (Suggested by Author(s))	18. Distribution Statement
Electric propulsion Magnetoplasmadynamics	Unclassified - Unlimited Subject Category 20

19. Security Classif. (of the report)	20. Security Classif. (of this page)	21. No. of pages	22. Price*
Unclassified	Unclassified	36	A03

NASA FORM 1626 OCT 86

*For sale by the National Technical Information Service, Springfield, Virginia 22161